*Egypt. J. Chem.* **Vol. 67**, No. 9 pp. 613 - 636 (2024)

**Egyptian Journal of Chemistry**

**http://ejchem.journals.ekb.eg/**

# Assessing Structural Characterization of Novel Nano Organometallic Complexes against Divergent Microbes

**Mohammed Kaid*[a], Abdou Saad El-Tabl[a], Moshira Mohamed Abd-El Wahed[c], RehamWagdy Farid[b] and Awatef Abd Elsalam Masoud[b]**

[a] Department of Chemistry, Faculty of Science, El-Menoufia University, Shebin El -Kom, Egypt
[b] Department of Chemistry, Faculty of Science, Tobruk University, Libya
[c] Department of Pathology, Faculty of Medicine, El-Menoufia University, Shebin El-Kom, Egypt

**Abstract**

The escalating prevalence of multidrug resistance (MDR) worldwide has spurred a critical imperative to explore and innovate novel therapeutic modalities and potent antimicrobial agents. Amide Schiff-base ligands (referred to as $H_3L_1$ and $H_3L_2$) have emerged as promising candidates for combating a spectrum of pathogens including Gram-negative bacteria, Gram-positive bacteria, and certain antifungal strains, amid the scarcity of novel antibiotics. Concurrently, β-naphthylamide (PAβN), a peptidomimetic compound, has garnered attention as an efflux pump inhibitor (EPI) aimed at surmounting efflux-mediated multidrug resistance. In this investigation, the antibacterial efficacy of two Schiff base ligands synthesized through the condensation of (N-(2-amino phenyl)-2-hydroxybenzamide) with hydroxybenzaldehyde, and (N-(2-aminoethyl)-2-hydroxybenzamide) with hydroxybenzaldehyde, alongside their respective complexes $[H_3L_1.Cu(OAc)_2].2H_2O$, $[H_3L_1CuCl_2].2H_2O$, $[H_3L_1Ag_2(SO_4)]$, $[H_3L_1Hg(SO_4)(H_2O)]\cdot 2H_2O$, $[H_3L_2Cu(OAc)_2]\cdot 2H_2O$, and $[H_3L_2CuCl_2]\cdot 3H_2O$). The ligands and their complexes were characterized using elemental and spectroscopic techniques such as IR, UV-VIS, Mass Spectra, $^1$H-NMR and ESR measurements as well as Magnetism, Conductivity, Thermal Analyses (DTA and TGA) and Electronic microscope. The conductivity measurements confirmed non electrolytic in nature, however, The electron microscope data indicate that, the complexes were found in nano-form. ESR spectra for Cu(II) complexes showed axial type with $d(x^2-y^2)$ ground state. The compounds were assessed individually against a spectrum of bacteria including Escherichia coli (ATCC:10536), Klebsiella pneumoniae (ATCC:10031), Staphylococcus aureus (ATCC:13565), Streptococcus mutans (ATCC:25175), and Candida albicans (ATCC:10231), encompassing antibiotic-susceptible strains. Preliminary results of minimum inhibition concentration (MIC) assays revealed notable antimicrobial activity exhibited by the complexes $[H_3L_1.Cu(OAc)_2].2H_2O$, $[H_3L_1CuCl_2].2H_2O$, $[H_3L_1Ag_2(SO_4)]$, $[H_3L_1Hg(SO_4)(H_2O)]\cdot 2H_2O$, $[H_3L_2Cu(OAc)_2]\cdot 2H_2O$, and $[H_3L_2CuCl_2]\cdot 3H_2O$) when compared to the ligands in isolation. Further analysis via fractional inhibitory concentration (FIC) indices demonstrated enhanced MIC values indicative of additive and synergistic effects upon combining NANO METAL AMIDE SCHIFF BASE complexes with $H_3L_1$ and $H_3L_2$. These findings underscore the therapeutic promise inherent in the combined utilization of NANO METAL AMIDE SCHIFF BASE COMPLEXES with $H_3L_1$ and $H_3L_2$.

*KEYWORDS: Hydroxy Schiff – bases , complexes, spectra, magnetism, Thermal analyses, Antimicrobial activity*

## 1. Introduction

The World Health Organization (WHO) has identified an alarming increase in the prevalence of multidrug resistance (MDR) among bacteria, a concerning trend that undermines the effectiveness of numerous antibiotics. Annually, approximately 23,000 fatalities in the United States alone are attributed to antibiotic-resistant infections, highlighting the grave implications of this issue. Similarly, Malaysia has witnessed a consistent uptick in cases of antibiotic resistance, mirroring global concerns [1]. The emergence of antibiotic resistance is a multifaceted phenomenon with complexes [2] patterns circulating within various contexts. Bacterial strains including Escherichia coli (E. coli), Klebsiella pneumoniae (K. pneumoniae), Staphylococcus aureus (S. aureus), and numerous others exhibit escalating levels of resistance

*Corresponding author e-mail: mohamed.kayed23@science.menofia.edu.eg, (Mohammed Kaid)
Received date 16 March 2024; revised date 13 July 2024; accepted date 14 July 2024
DOI: 10.21608/ejchem.2024.276694.9448
©2024 National Information and Documentation Center (NIDOC)

[3]. This concerning trend has prompted urgent collaborative efforts among scientists and healthcare researchers to explore novel therapeutic approaches and potent medications capable of addressing the challenge posed by multidrug resistance (MDR). Polymyxins, initially isolated in 1947 from various Bacillus polymyxa species, constitute a group of cationic polypeptides [4]. Sharing structural and mechanistic similarities with cationic antimicrobial peptides (CAMPs) like defensins, polymyxins target and disrupt the outer membrane integrity of Gram-negative bacteria, rendering them susceptible to antibiotics. The polymyxin family encompasses five members, namely polymyxin A, B, C, D, and E [5]. However, only polymyxin B (available as sulfate salt) and polymyxin E (also known as colistin) are clinically employed, serving as last-resort therapies for combating life-threatening infections induced by Gram-negative pathogens, notably Pseudomonas aeruginosa [6, 7] (P. aeruginosa) and Acinetobacter baumannii (A. baumannii), both categorized as "Priority 1: Critical" pathogens in the 2017 WHO Priority Pathogen List [8]. Efflux pumps, integral membrane proteins, play a pivotal role in antimicrobial resistance by expelling detrimental cellular substances such as antibiotics, toxins, and metabolic by-products from bacteria into the external milieu. Notably, various superfamilies of efflux pumps, including multidrug and toxin extrusion (MATE), small multidrug resistance (SMR), major facilitator superfamily (MFS), ATP-binding cassette (ABC), and resistance-nodulation division (RND), contribute to MDR [7, 9]. Researchers have identified efflux pumps belonging to the RND family in Gram-negative strains such as P. aeruginosa and E. coli, while Gram-positive bacteria like S. aureus commonly feature MFS (e.g., NorA) and ABC transporters [10]. Phenylalanine-arginine β-naphthylamide (PAβN), an extensively researched efflux pump inhibitor (EPI), has demonstrated efficacy in thwarting bacterial efflux pumps' ability to expel antibiotics through various mechanisms. It can competitively inhibit efflux pumps by binding to them, or through steric hindrance during binding, impeding antibiotics from accessing their target sites [11]. Combination therapy offers several advantages, including the prevention of resistance development and reduction in drug doses or treatment durations [5]. For instance, combining polymyxins with other agents exploits their ability to disrupt Gram-negative bacteria's outer membrane integrity, thereby enhancing the efficacy of adjunctive drugs [12].The combination of polymyxin B nonapeptide with Schiff bases derived from S-benzyl dithiocarbazate (SBDTC), such as SB4CB and $Cu(SB4CB)_2$, demonstrated enhanced antibacterial properties against several strains including A. baumannii ATCC 19606, K. pneumoniae ATCC 11296, P. aeruginosa PA01, Salmonella enterica SL696, and S. aureus SA1199. Likewise observed improved antibacterial activity of various antibiotics when used in conjunction with PaβN [13]. Notably, the presence of 25 μg/mL PAβN reduced the MIC values of vancomycin from > 256 to 96 μg/mL for both wild type and dacB strains of P. aeruginosa, with further reductions to 32 μg/mL observed with 50 μg/mL PAβN. This enhancement in susceptibility was attributed not only to PAβN's efflux inhibition but also to its permeabilizing effect on the bacterial outer membrane. The origin of Schiff bases traces back to 1864 when synthetic chemist Hugo Schiff successfully synthesized a class of compounds containing azomethine or imine functional groups, which came to be known as Schiff bases [6, 14]. These compounds are synthesized through the condensation of primary amines with aldehydes or ketones. Over the years, numerous studies have highlighted the potential of Schiff bases and their metal complexes in designing novel antibacterial therapeutics . Among these, copper (Cu) ions have garnered significant interest due to their excellent therapeutic potential. It has demonstrated that Cu(II) complexes of morpholine-derived Schiff base ligands exhibited superior antibacterial activity compared to the corresponding Schiff base ligands and the standard drug amikacin [15, 16]. This underscores the importance of chelation in facilitating the crossing of cell membranes by metal complexes. Similar enhancements in antimicrobial activity have been observed for Cu(II) Schiff base complexes against various pathogens, including anaerobic bacteria [17]. Moreover, Cu(II) Schiff base complexes have been explored for their anticancer, anti-inflammatory, antifungal, and positron emission tomography (PET) hypoxia imaging properties [10, 18, 19]. Therefore, in this study, we evaluated the antibacterial potential of synthesized Schiff bases and their Cu(II) complexes against eight bacterial isolates, including both susceptible and resistant strains of S. aureus, P. aeruginosa, E. coli, and A. baumannii, building upon previous research on S-benzyl dithiocarbazate (SBDTC)-derived Schiff bases [5, 20]. In the realm of ligands and Cu(II) complexes, even subtle structural alterations can significantly impact bioactivity. For instance, the addition of a hydroxyl (-OH) group to 4-formyl-3-hydroxybenzoic acid, yielding SBFH and $Cu(SBFH)_2$, garnered interest based on prior research indicating that compounds featuring hydroxyl groups exhibit potent antimicrobial properties [21]. In pursuit of optimizing antimicrobial efficacy, combination tests were conducted, pairing the most promising compound, $Cu(SBFH)_2$, with POLY and PAβN. Moreover, to corroborate the findings of in vitro antibacterial studies, molecular docking investigations were undertaken. These studies aimed to elucidate the binding modes and interactions of the compound

within the active sites of efflux pumps, shedding light on the molecular recognition of ligands within the binding pocket.

## 2. Materials and methods Synthesis

### 2.1. Materials and instrumentations

All reagents and solvents utilized in this study were of analytical grade. These included used metal salts, dimethyl sulfoxide (DMSO) and acetonitrile (ACN) obtained from Fisher Chemicals. Fourier-transform infrared (FTIR) spectra were meticulously recorded within the range of 400–4000 $cm^{-1}$ using a Shimadzu IRAffinity-1S FTIR spectrophotometer, operating in attenuated total reflection (ATR) mode [20]. Each spectrum was acquired over 20 total scans with four resolution settings. The acquired spectra were subsequently saved and analyzed using ORIGIN software. Elemental analysis data were procured employing the LECO MicroTruspec CHNS Elemental Analyzer, available at Universiti Malaya, to ascertain the elemental composition of the compounds under investigation. UV–Visible spectra were acquired using a Perkin Elmer Lambda 25 UV/VIS spectrophotometer equipped with a quartz cuvette featuring a 1 cm optical path. Additionally, $^1$H Nuclear Magnetic Resonance (NMR) spectra was recorded using a Bruker DRX300 instrument to provide insights into the molecular structure and chemical environment of the compounds studied [22].

### 2.2. Preparation of the ligands and their metal complexes.

#### 2.2.1. Preparation of Schiff-base ligand ($H_3L_1$)

1- Synthesis of (N-(2-amino phenyl)-2-hydroxybenzamide). The ligand, denoted as $H_3L_1$, was synthesized in two sequential steps: First, salicylic acid (20.0 g, 0.13 mol) was added dropwise to 30 $cm^3$ of ethyl alcohol, initiating esterification to yield ethyl-2-hydroxybenzoate. In the second step, the resulting ethyl-2-hydroxybenzoate was combined with benzen-1,2-diamine (29.0 g, 0.26 mol) dissolved in 20 $cm^3$ of ethanol solution. The mixture was refluxed with stirring for 2 hours, followed by cooling to room temperature. The precipitate formed was filtered off and left to dry at ambient conditions, resulting in the formation of (N-(2-amino phenyl)-2-hydroxybenzamide).

2- Synthesis of Schiff-base Ligand $H_3L_1$ An ethanolic solution containing the synthesized product (N-(2-amino phenyl)-2-hydroxybenzamide) (24.0 g, 0.08 mol) was added to 2-hydroxybenzaldehyde (22.9 g, 0.17 mol) in a 1:2 ratio, dissolved in 30 $cm^3$ of ethanol. The resulting mixture was stirred and refluxed for an additional two hours at 60-70 $^0$C, followed by cooling to room temperature. The solid product was then filtered, and subsequently dried under vacuum conditions using anhydrous $CaCl_2$ to obtain the ligand. Analytical data pertaining to the ligand are presented in Table 1, and the synthetic pathway is depicted in scheme (1).

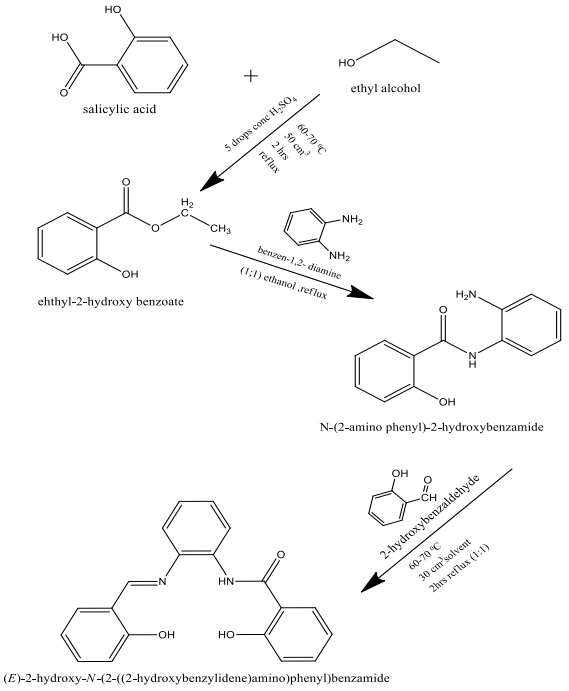


scheme (1): preparation of Schiff-base ligand ($H_3L_1$)

#### 2.2.2. Preparation of Schiff-base ligand (H3L2)

1- The synthesis of N-(2-aminoethyl)-2-hydroxybenzamide, designated as $H_3L_2$, involved two consecutive steps:
Firstly, salicylic acid (20.0 g, 0.13 mol) was added dropwise to 30 $cm^3$ of ethyl alcohol to undergo esterification, resulting in the formation of ethyl-2-hydroxybenzoate.
Secondly, the obtained ethyl-2-hydroxybenzoate was combined with ethane-1,2-diamine (29.0 g, 0.26 mol) dissolved in 20 $cm^3$ of ethanol solution to form a hydrazone. The mixture was refluxed with stirring for 2 hours and then allowed to cool to room temperature. The precipitate formed was filtered off and air-dried at room temperature, yielding N-(2-aminoethyl)-2-hydroxybenzamide.

2- synthesize the Schiff-base ligand ($H_3L_2$), a solution of N-(2-aminoethyl)-2-

hydroxybenzamide (24.0g, 0.08 mol) in ethanol was combined with 2-hydroxybenzaldehyde (22.9g, 0.17 mol) at a 1:2 ratio in a 30 $cm^3$ ethanol solvent. The resulting mixture was stirred and refluxed for two hours at 60-70 $^{O}C$, followed by cooling to room temperature. The precipitated solid product was filtered, then dried under vacuum using anhydrous $CaCl_2$. The ligand was obtained as a result. Analytical data for the ligand are presented in Table 1, and the synthesis procedure is illustrated in Scheme 2.

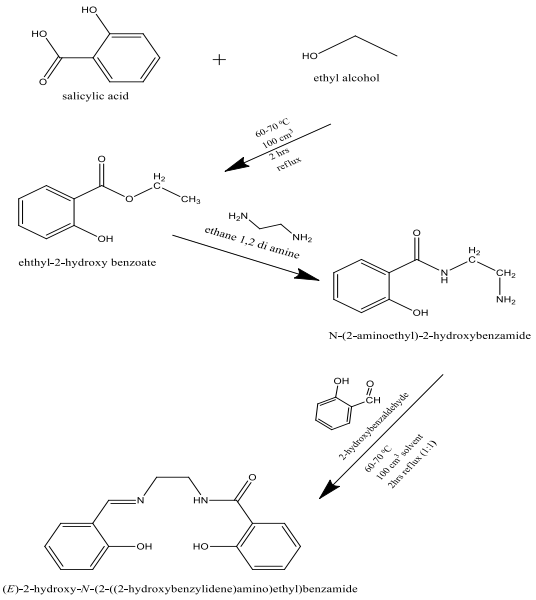


Scheme (2): preparation of Schiff-base ligand $H_3L_2$

### 2.2.3. Synthesis of metal complexes

1- Synthesis of metal complexes, (1-2-3-4) $H_3L_1$

The metal complexes (1,2,3,4) were synthesized by refluxing a 30 $cm^3$ hot ethanolic solution containing 1.0g (0.003 mol) of the ligand ($H_3L_1$) with a 30 $cm^3$ hot ethanolic solution of the respective metal salts: $Cu(OAc)_2].2H_2O$ (0.64 g, 0.003 mol) for complex (1), $H_3L_1CuCl_2].2\ H_2O$ (1.01g, 0.003 mol) for complex (2), $Ag_2(SO_4)]$ (1.25 g, 0.003 mol) for complex (3), and $Hg(SO_4)(\ H_2O)].2\ H_2O$ (0.8g, 0.003 mol) for complex (4). The molar ratios for ligands to metal salts were maintained at 1:1. The reaction mixtures were refluxed with stirring for a duration ranging from 1 to 3 hours, depending on the specific metal ion and anion involved. The resulting precipitates were filtered, washed with ethanol, and subsequently dried in desiccators containing anhydrous $CaCl_2$.

### 2.2.4. Synthesis of metal complexes, (5-6) H3L2

The metal complexes (5-6) were synthesized by refluxing a 30 $cm^3$ hot ethanolic solution containing 1.0g (0.003 mol) of the ligand ($H_3L_2$) with a 30 $cm^3$ hot ethanolic solution of the respective metal salts: $Cu(OAc)_2].2H_2O$ (1.54 g, 0.003 mol) for complex (5) and $CuCl_2].3\ H_2O$ (0.64 g, 0.003 mol) for complex (6). The molar ratios for ligands to metal salts were maintained at 1:1. The reaction mixtures were refluxed with stirring for a duration ranging from 1 to 3 hours, adjusted according to the specific metal ion and anion involved. Subsequently, the resulting precipitates were separated by filtration, washed with ethanol, and dried in desiccators containing anhydrous $CaCl_2$.

## 3. Biological studies

### 3.1. Antimicrobial assay

The antimicrobial activity of the compounds under investigation was assessed utilizing the agar well diffusion method. In vitro testing for antibacterial efficacy involved examining the compounds against Gram-positive bacteria such as Staphylococcus aureus and Streptococcus mutans, as well as Gram-negative bacteria including Escherichia coli, Pseudomonas aeruginosa, and Klebsiella pneumonia, using nutrient agar medium. Similarly, the antifungal activity of the compounds was evaluated against Candida albicans and Aspergillus niger using Sabouraud dextrose agar medium. Standard drugs, including Ampicillin and Gentamicin for Gram-positive and Gram-negative bacteria, respectively, and Nystatin for fungal strains, were employed for comparison. DMSO served as the negative control solvent. The compounds were tested at a concentration of 15 mg/ml against both bacterial and fungal strains [22].

### 3.2. Method of testing

The sterilized nutrient agar media was carefully poured into sterile Petri dishes (20-25 ml per dish) and left to solidify at room temperature. A microbial suspension was prepared in sterilized saline to match the McFarland 0.5 standard solution (equivalent to 1.5x 105 CFU $mL^{-1}$), and its turbidity was adjusted to OD= 0.13 using a spectrophotometer set at 625 nm wavelength. Ideally, within 15 minutes of turbidity adjustment, a sterile cotton swab was immersed into the prepared suspension and then gently spread over the surface of the dried agar in each Petri dish. Afterward, the plates were left undisturbed for 15 minutes with their lids on [23]. Wells, each with a diameter of 6 mm, were carefully created in the solidified agar using a sterile borer. Next, 100 µL of the compound solution being tested was added to each well using a micropipette. The plates were then incubated at 37°C for 24 hours to assess antibacterial

activity. This experimental procedure was performed in triplicate, and the resulting zones of inhibition were measured in millimeters.

## 4. Results and discussion

### 4.1. Synthesis and characterisations

The combination of Schiff-base ligands with various metal salts at a 1:1 ratio initiates a fascinating journey into the realm of coordination chemistry, leading to the creation of diverse complexes. These resultant metal complexes, with their vivid and distinctive colors, stand as crystalline solids, emblematic of their robust stability at ambient conditions, steadfastly resisting decomposition over prolonged durations. Remarkably, these complexes exhibit insolubility in a plethora of common solvents such as water, ethanol, methanol, benzene, toluene, acetonitrile, and chloroform, yet they display appreciable solubility when immersed in the realms of dimethylformamide (DMF) and dimethylsulfoxide (DMSO), a testament to their intriguing chemical behavior. Elemental analyses, serving as the bedrock of confirmation, validate the consistent 1:1 molar ratio composition of all synthesized complexes, instilling confidence in their structural integrity. A meticulous process of characterization unfolds, encompassing a myriad of analytical techniques such as elemental and spectral analyses including IR, UV-VIS, mass spectra, $^1$HNMR, and ESR, supplemented by electrical conductivity assessments, magnetic measurements, and thermal analyses (DTA and TGA). The culmination of these endeavors, both analytical and physical, is encapsulated within the comprehensive data showcased in Table 1, elucidating the intrinsic properties of the complexes. Meanwhile, the spectral data, meticulously cataloged in Tables 2-6, seamlessly align with the proposed structures, as elegantly illustrated in Figure 17, providing a visual narrative of molecular orchestration [24]. The molar conductance of these enigmatic complexes, meticulously measured in $10^{-3}$ M DMF at 25°C, unveils a fascinating insight, as depicted in Table 1, Show casing a range from 4.45 to 8.64 ohm$^{-1}$ cm$^2$ mol$^{-1}$, a characteristic hallmark of their non-electrolytic nature, further underscoring their unique chemical behavior. In the intricate dance of molecular synthesis, stands as a testament, encapsulating the intricate choreography between the ligands and their respective metal salts, immortalizing the transformative journey from reactants to products in the annals of chemical discovery.

**Table 1:** Analytical and Physical Data of the Ligands [$H_3L_1$], [$H_3L_2$] and their Metal Complexes.

| No. | Ligand/Complexes | Color | FW | M.P (OC) | Yield (%) | Anal. /Found (Calc.) (%) | | | Molar conductance* |
|---|---|---|---|---|---|---|---|---|---|
| | | | | | | C | H | N | |
| (1) | $[H_3L_1.Cu(OAc)_2].2H_2O$ | Brown | 549 | >300 | 79 | P:53.20 Th:53.99 | P:4.30 Th:4.50 | P:5.40 Th:5.73 | 6.4 |
| (2) | $[H_3L_1CuCl_2].2\ H_2O$ | Brown | 501 | >300 | 75 | P:53.66 Th:53.69 | P:4.27 Th:4.47 | P:6.54 Th:6.26 | 7.3 |
| (3) | $[H_3L_1Ag_2(SO_4)]$ | Black/Brown | 642 | >300 | 70 | P:36.79 Th:37.2 | P:2.39 Th:2.48 | P:4.88 Th:4.34 | 5.8 |
| (4) | $[H_3L_1Hg(SO_4)(\ H_2O)].2\ H_2O$ | Greenish black | 684 | >300 | 76 | P:44.80 Th:45.02 | P:2.31 Th:2.6 | P:4.92 Th:5.2 | 5.6 |
| (5) | $[H_3L_2\ Cu(OAc)_2].2H_2O$ | Green | 501 | >300 | 75 | P:48.71 Th:49.09 | P:4.82 Th:5.0 | P:6.11 Th:6.36 | 4.45 |
| (6) | $[H_3L_2\ CuCl_2].3\ H_2O$ | Brown | 471 | >300 | 70 | P:47.72 Th:48.24 | P:4.78 Th:5.02 | P:6.82 Th:7.03 | 4.77 |

*$\Lambda m(\Omega^{-1}cm^2mol^{-l})$

### 4.2. Molar Conductivity

The molar conductivity of the metal complexes was assessed in a DMSO solvent at a concentration of $10^{-3}$ M. The recorded molar conductivity values, delineated in Table 1, indicate relatively low conductivity, expressed in $\Omega^{-1}cm^2mol^{-1}$. These values are indicative of the non-electrolytic behavior exhibited by all complexes [23]. Such outcomes align seamlessly with the analytical findings, implying the involvement of anionic groups in the process of metal coordination. This correlation reinforces the notion that the complexes possess a predominantly covalent character, wherein the charge transfer phenomena are subdued, thereby underscoring their stable molecular architecture.

### 4.3. $^1$H-NMR Spectra

The $^1$H-NMR spectra of ligand [$H_3L_1$] Chart (1), dissolved in deuterated DMSO provide insights consistent with the proposed molecular structures. In the spectrum, a singlet appearing at 5.5 ppm (S, H, OH) signifies the presence of the proton associated

with the aromatic hydroxyl group within ligand (1). Furthermore, resonances observed at 3.8 ppm are attributed to the azomethine protons (H-C=N), while a singlet at 8.1 ppm corresponds to the NH group proton. Multiple signals spanning the range of 6.8-7.4 ppm indicate the presence of protons belonging to aromatic rings within the ligand's structure. Similarly, in the case of ligand [$H_3L_2$] Chart (2), the $^1$H-NMR spectra in deuterated DMSO reflect characteristics consistent with the proposed molecular configuration. Resonances at 2.4 and 3.9 ppm are ascribed to ($CH_2$) protons within ligand (2), while a singlet at 11.8 ppm corresponds to the proton associated with the aromatic hydroxyl group. Additionally, chemical shifts at 3.90 ppm are attributed to the azomethine protons (H-C=N), with a singlet at 10.28 ppm representing the NH group proton. Multiplet signals spanning 6.9-7.8 ppm signify the presence of protons originating from aromatic rings within the ligand's structure. These spectral observations, meticulously recorded and analyzed, provide valuable corroborative evidence supporting the proposed structural compositions of both ligands. The resonance patterns observed align precisely with the expected chemical environments and bonding configurations within the ligand molecules, validating the integrity of the proposed molecular structures. Such detailed spectroscopic characterization serves as a cornerstone in elucidating the intricate chemical architecture of these ligands, laying a solid foundation for further exploration and understanding of their reactivity and coordination behavior in the formation of metal complexes.

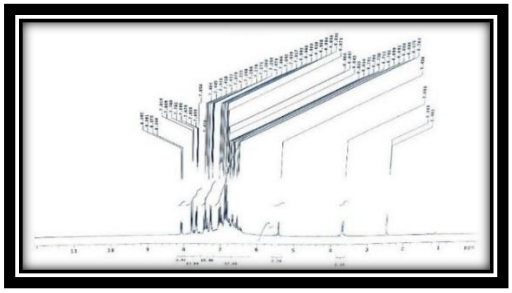

**Chart** 1: $^1$H-NMR spectrum of the ligand [$H_3L_1$]

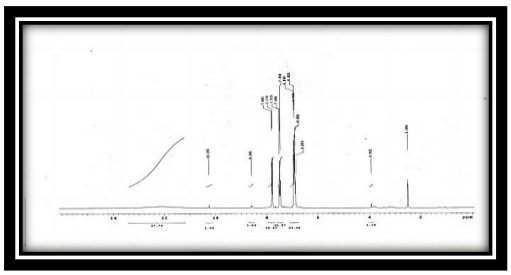

**Chart 2:** $^1$H-NMR spectrum of the ligand [$H_3L_2$]

### 4.4. Mass spectra

Mass spectrometry was used to confirm the molecular ion peaks of $H_3L_1$ Schiff base and investigate the fragment species [25]. The recorded mass spectrum of $H_3L_1$ ligand revealed molecular ion peak confirms strongly the proposed formula. It showed a molecular ion peaks : With an m/z value of 52, the fragment is denoted by the molecular formula $C_4H_4$, signifying a four-carbon hydrocarbon. At m/z 68, the presence of an oxygen atom is indicated alongside the four-carbon hydrocarbon, described by the molecular formula $C_4H_4O$. Representing a six-carbon hydrocarbon fragment, m/z 76 is identified as $C_6H_4$. At m/z 93, the fragment with the molecular formula $C_6H_5O$ suggests the inclusion of a phenyl group ($C_6H_5$) with an additional oxygen atom. Corresponding to a seven-carbon hydrocarbon with an oxygen atom, m/z 106 is expressed as $C_7H_6O$. M/z 120 suggests a seven-carbon hydrocarbon with the presence of both nitrogen and oxygen, denoted by the molecular formula $C_7H_6NO$. Indicating a seven-carbon hydrocarbon with a nitrogen and two oxygen atoms, m/z 136 is represented by the formula $C_7H_6NO_2$. At m/z 145, the fragment is identified as a nine-carbon hydrocarbon with a nitrogen and an oxygen atom, expressed as $C_9H_7NO$. Corresponding to a ten-carbon hydrocarbon with a nitrogen and an oxygen atom, m/z 158 is denoted as $C_{10}H_8NO$. M/z 184 suggests a twelve-carbon hydrocarbon with a nitrogen and an oxygen atom, represented by the formula $C_{12}H_{10}NO$. Representing a thirteen-carbon hydrocarbon with two nitrogen atoms and an oxygen atom, m/z 211 is expressed as $C_{13}H_{11}N_2O$. Indicating a thirteen-carbon hydrocarbon with two nitrogen atoms and two oxygen atoms, m/z 226 is represented by the formula $C_{13}H_{10}N_2O_2$. M/z 280 corresponds to a sixteen-carbon hydrocarbon with three oxygen atoms and two nitrogen atoms, expressed as $C_{16}H_{12}N_2O_3$. Representing a seventeen-carbon hydrocarbon with three oxygen atoms and two nitrogen atoms, m/z 293 is expressed as $C_{17}H_{13}N_2O_3$. At m/z 315, the fragment is indicative of a twenty-carbon hydrocarbon with three oxygen atoms and two nitrogen atoms, denoted as $C_{20}H_{15}N_2O_3$. Corresponding to a twenty-carbon hydrocarbon with two nitrogen atoms and two oxygen atoms, m/z 316 is expressed as $C_{20}H_{16}N_2O_2$. M/z 332 represents a twenty-carbon hydrocarbon with three oxygen atoms and two nitrogen atoms, expressed as $C_{20}H_{16}N_2O_3$. These interpretations facilitate an understanding of the molecular composition of detected fragments in the mass spectra data, supported the suggested structure of the ligand (1) [(Table 2, chart 3]. Also, Mass spectrometry was used to confirm the molecular ion peaks of $H_3L_2$ Schiff -base and investigate the fragment species. The recorded mass spectrum of $H_3L_2$ ligand revealed molecular ion peak confirms strongly the proposed formula. It showed a molecular ion peak: At m/z 52, a fragment with a mass of 52 is observed, indicating a molecule with the composition $C_4H_4$. At m/z 68, a fragment with a mass

of 68 is present, corresponding to a molecule with the composition $C_4H_4O$. The mass spectrum shows a fragment at m/z 93, suggesting a molecule with the composition $C_6H_5O$. At m/z 106, a fragment with a mass of 106 is observed, indicating a molecule with the composition $C_7H_6O$. A fragment with a mass of 120 at m/z suggests a molecule with the composition $C_7H_6NO$. At m/z 134, a fragment with a mass of 134 is present, indicating a molecule with the composition $C_8H_8NO$. The presence of a fragment at m/z 136 suggests a molecule with the composition $C_7H_6NO_2$. At m/z 163, a fragment with a mass of 163 is observed, indicating a molecule with the composition $C_9H_{11}N_2O$. A fragment with a mass of 191 at m/z suggests a molecule with the composition $C_{10}H_{11}N_2O_2$. At m/z 204, a fragment with a mass of 204 is present, corresponding to a molecule with the composition $C_{11}H_{12}N_2O_2$. A fragment with a mass of 216 at m/z suggests a molecule with the composition $C_{12}H_{12}N_2O_2$. At m/z 258, a fragment with a mass of 258 is observed, indicating a molecule with the composition $C_{14}H_{14}NO_3$. The presence of a fragment at m/z 267 suggests a molecule with the composition $C_{14}H_{14}N_2O_2$. At m/z 284, a fragment with a mass of 284 is present, corresponding to a molecule with the composition $C_{16}H_{16}N_2O_3$. These detailed explanations supported the suggested structure of the ligand [Table 3, chart 4].

**Table 2:** Mass spectrum of Ligands [$H_3L_1$].

| m/z | Fragment |
|---|---|
| 52 | $C_4H_4$ |
| 68 | $C_4H_4O$ |
| 76 | $C_6H_4$ |
| 93 | $C_6H_5O$ |
| 106 | $C_7H_6O$ |
| 120 | $C_7H_6NO$ |
| 136 | $C_7H_6NO_2$ |
| 145 | $C_9H_7NO$ |
| 158 | $C_{10}H_8NO$ |
| 184 | $C_{12}H_{10}NO$ |
| 211 | $C_{13}H_{11}N_2O$ |
| 226 | $C_{13}H_{10}N_2O_2$ |
| 280 | $C_{16}H_{12}N_2O_3$ |
| 293 | $C_{17}H_{13}N_2O_3$ |
| 315 | $C_{20}H_{15}N_2O_3$ |
| 316 | $C_{20}H_{16}N_2O_2$ |
| 332 | $C_{20}H_{16}N_2O_3$ |

**Table 3:** Mass spectrum of Ligands [$H_3L_2$].

| m/z | Fragment |
|---|---|
| 52 | $C_4H_4$ |
| 68 | $C_4H_4O$ |
| 93 | $C_6H_5O$ |
| 106 | $C_7H_6O$ |
| 120 | $C_7H_6NO$ |
| 134 | $C_8H_8NO$ |
| 136 | $C_7H_6NO_2$ |
| 163 | $C_9H_{11}N_2O$ |
| 191 | $C_{10}H_{11}N_2O_2$ |
| 204 | $C_{11}H_{12}N_2O_2$ |
| 216 | $C_{12}H_{12}N_2O_2$ |
| 258 | $C_{14}H_{14}NO_3$ |
| 267 | $C_{14}H_{14}N_2O_2$ |
| 284 | $C_{16}H_{16}N_2O_3$ |

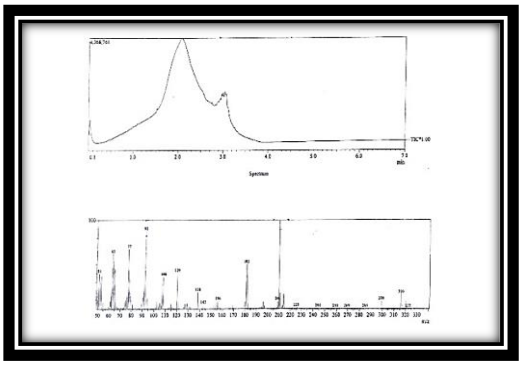

**Chart 3:** Mass spectrum of ligand[$H_3L_1$]

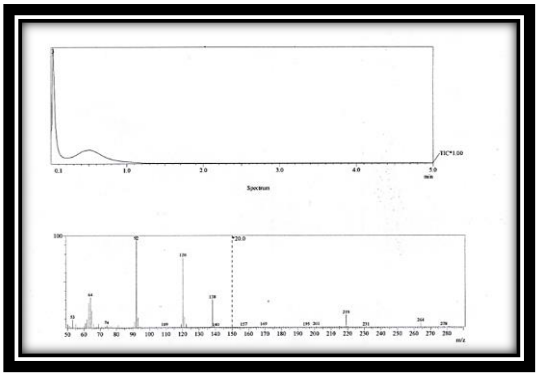

**Chart 4:** Mass spectrum of ligand[H3L2]

### 4.5. IR Spectra

The bonding of the ligand to the metal ions has been judged by a careful comparison of the infrared spectra of the metal complexes

with those of the free ligand. A few significant bands have been selected to observe the effect on vibrations of the ligand's groups upon complexation as showed in (Table 4). The characteristic Infrared spectral data of ligand $H_3L_1$ and its metal chelates are listed in (Table 4). The spectra of the ligand and its metal chelates showed characteristics absorption. The provided IR spectra data corresponds to ligand $H_3L_1$, and the absence of specific information in certain regions suggests the potential presence or absence of certain functional groups. Here's a discussion of the given data:n ν($H_2O$): No specific peaks are provided in the ν($H_2O$) region. This implies that there is no distinctive water absorption observed in the IR spectrum, indicating that the compound is not significantly hydrated, ν(OH): Peaks at 3451, 3400, and 1294 $cm^{-1}$ are indicative of the hydroxyl (OH) group. The higher-frequency peaks suggest the presence of free hydroxyl groups, while the lower-frequency peak may indicate hydrogen-bonded hydroxyl groups. υ(H-bonding): A peak at 1640 $cm^{-1}$ is observed, indicating the presence of hydrogen bonding. This absorption is characteristic of compounds where hydrogen atoms are involved in hydrogen bonding interactions. ν(C=O): A peak at 3280 $cm^{-1}$ suggests the presence of a carbonyl (C=O) group. The specific nature of the carbonyl functionality (e.g., ketone, aldehyde) is not provided. ν(C=N): A peak at 1625 $cm^{-1}$ is attributed to the azomethine (C=N) functional group. This indicates the presence of a nitrogen-carbon double bond in the compound. ν(N-O): Peaks at 1456, 756, and 1400 $cm^{-1}$ are associated with the nitro (N-O) group. These peaks suggest the stretching vibrations of nitrogen-oxygen bonds within the nitro group. ν(Ar): No specific peaks are provided in the ν(Ar) region. The provided IR spectra data corresponds to Compound (1), represents specific vibrational modes associated with various functional groups within the compound. Let's discuss the information provided: ν($H_2O$): Peaks at 3550, 3250, 3230, and 2940 $cm^{-1}$ indicate the presence of water. These peaks suggest stretching vibrations of water molecules within the compound. ν(OH): Peaks at 3409, 3389, and 1246 $cm^{-1}$ represent the hydroxyl (OH) group. The higher-frequency peaks indicate the stretching vibrations of free hydroxyl groups, while the lower-frequency peak may indicate hydrogen-bonded hydroxyl groups. υ(H-bonding): Peaks at 3615, 3375, 3270, and 2885 $cm^{-1}$ suggest the involvement of hydrogen bonding. These peaks are characteristic of compounds where hydrogen atoms are engaged in hydrogen bonding interactions. ν(C=O): A peak at 1650 $cm^{-1}$ indicates the presence of a carbonyl (C=O) group. The specific nature of the carbonyl functionality (e.g., ketone, aldehyde) is not provided. ν(C=N): A peak at 3200 $cm^{-1}$ is attributed to the azomethine (C=N) functional group, indicating the presence of a nitrogen-carbon double bond in the compound. ν(N-O): A peak at 1609 $cm^{-1}$ corresponds to the nitro (N-O) group, suggesting stretching vibrations of nitrogen-oxygen bonds within the nitro group. ν(Ar): Peaks at 1455, 752, and 1470 $cm^{-1}$ suggest the presence of aromatic rings. These peaks are associated with stretching vibrations of the aromatic C-H bonds. ν(OAc): Peaks at 1405 and 1365 $cm^{-1}$ suggest the presence of acetate (OAc) groups. These peaks are associated with specific stretching vibrations of these functional groups. υ(M-O): A peak at 672 $cm^{-1}$ indicates metal-oxygen stretching vibrations. This suggests the possible coordination of a metal ion with oxygen atoms in the compound. υ(M-N): A peak at 531 $cm^{-1}$ corresponds to metal-nitrogen stretching vibrations. This implies the involvement of a metal-nitrogen coordination bond within the compound. In summary, the IR spectra data for Compound (1) indicates the presence of water, hydroxyl, carbonyl, azomethine, nitro, aromatic, acetate, groups. Hydrogen bonding and metal coordination are suggested by specific peaks in the spectrum. The detailed information regarding various functional groups enhances the characterization of Compound (1). The provided IR spectra data corresponds to Compound (2), represents specific vibrational modes associated with various functional groups within the compound. Let's discuss the information provided: ν($H_2O$): Peaks at 3475, 3310, 3300, and 3090 $cm^{-1}$ indicate the presence of water. These peaks suggest stretching vibrations of water molecules within the compound. ν(OH): Peaks at 3448, 3395, and 1297, and 1243 $cm^{-1}$ represent the hydroxyl (OH) group. The higher-frequency peaks indicate the stretching vibrations of free hydroxyl groups, while the lower-frequency peak may indicate hydrogen-bonded hydroxyl groups. υ(H-bonding): Peaks at 3565, 3240, 3280, and 2710 $cm^{-1}$ suggest the involvement of hydrogen bonding. These peaks are characteristic of compounds where hydrogen atoms are engaged in hydrogen bonding interactions. ν(C=O): A peak at 1665 $cm^{-1}$ indicates the presence of a carbonyl (C=O) group. The specific nature of the carbonyl functionality (e.g., ketone, aldehyde) is not provided. ν(C=N): A peak at 3234 $cm^{-1}$ is attributed to the azomethine (C=N) functional group, indicating the presence of a nitrogen-carbon double bond in the compound. ν(N-O): A peak at 1610 $cm^{-1}$ corresponds to the nitro (N-O) group, suggesting stretching vibrations of nitrogen-oxygen bonds within the nitro group. ν(Ar): Peaks at 1535, 752, and 1480 $cm^{-1}$ suggest the presence of aromatic rings. These peaks are associated with stretching vibrations of the aromatic C-H bonds. ν(Cl): A peak at 466 $cm^{-1}$ suggests the presence of a functional group, possibly (Cl). However, more information is needed to confirm the specific group. υ(M-O): A peak at 665 $cm^{-1}$

indicates metal-oxygen stretching vibrations. This suggests the possible coordination of a metal ion with oxygen atoms in the compound. υ(M-N): A peak at 596 $cm^{-1}$ corresponds to metal-nitrogen stretching vibrations. This implies the involvement of a metal-nitrogen coordination bond within the compound. In summary, the IR spectra data for Compound (2) indicates the presence of water, hydroxyl, carbonyl, azomethine, nitro, aromatic, and possibly chloride. Hydrogen bonding and metal coordination are suggested by specific peaks in the spectrum. The detailed information regarding various functional groups enhances the characterization of Compound (2). The provided IR spectra data corresponds to Compound (3), represents specific vibrational modes associated with various functional groups within the compound. Let's discuss the information provided: ν(HO): Peaks at 3585, 3265, 3220, and 2998 $cm^{-1}$ indicate the presence of water. These peaks suggest stretching vibrations of water molecules within the compound. ν(OH): Peaks at 3410, 3285, 1300, and 1238 $cm^{-1}$ represent the hydroxyl (OH) group. The higher-frequency peaks indicate the stretching vibrations of free hydroxyl groups, while the lower-frequency peaks may indicate hydrogen-bonded hydroxyl groups. υ(H-bonding): Peaks at 3615, 3305, 3300, and 2465 $cm^{-1}$ suggest the involvement of hydrogen bonding. These peaks are characteristic of compounds where hydrogen atoms are engaged in hydrogen bonding interactions. ν(C=O): A peak at 1644 $cm^{-1}$ indicates the presence of a carbonyl (C=O) group. The specific nature of the carbonyl functionality (e.g., ketone, aldehyde) is not provided. ν(C=N): A peak at 3258 $cm^{-1}$ is attributed to the azomethine (C=N) functional group, indicating the presence of a nitrogen-carbon double bond in the compound. ν(N-O): A peak at 1602 $cm^{-1}$ corresponds to the nitro (N-O) group, suggesting stretching vibrations of nitrogen-oxygen bonds within the nitro group. ν(Ar): Peaks at 1498, 750, and 1465 $cm^{-1}$ suggest the presence of aromatic rings. These peaks are associated with stretching vibrations of the aromatic C-H bonds. ν($SO_4$): Peaks at 1105, 1038, 1050, and 690 $cm^{-1}$ suggest the presence of sulfate ($SO_4$), groups. These peaks are associated with specific stretching vibrations of these functional groups. υ(M-O): A peak at 613 $cm^{-1}$ indicates metal-oxygen stretching vibrations. This suggests the possible coordination of a metal ion with oxygen atoms in the compound. In summary, the IR spectra data for Compound (3) indicates the presence of water, hydroxyl, carbonyl, azomethine, nitro, aromatic, acetate, sulfate, chloride, or ammonium groups. Hydrogen bonding and metal coordination are suggested by specific peaks in the spectrum. The detailed information regarding various functional groups enhances the characterization of Compound (3). The provided IR spectra data corresponds to Compound (4), represents specific vibrational modes associated with various functional groups within the compound. Let's discuss the information provided: ν($H_2O$): Peaks at 3550, 3310, 3300, and 3095 $cm^{-1}$ indicate the presence of water. These peaks suggest stretching vibrations of water molecules within the compound. ν(OH): Peaks at 3427, 3385, 1355, and 1298 $cm^{-1}$ represent the hydroxyl (OH) group. The higher-frequency peaks indicate the stretching vibrations of free hydroxyl groups, while the lower-frequency peaks may indicate hydrogen-bonded hydroxyl groups. υ(H-bonding): Peaks at 3610, 3385, 3370, and 2455 $cm^{-1}$ suggest the involvement of hydrogen bonding. These peaks are characteristic of compounds where hydrogen atoms are engaged in hydrogen bonding interactions. ν(C=O): A peak at 1661 $cm^{-1}$ indicates the presence of a carbonyl (C=O) group. The specific nature of the carbonyl functionality (e.g., ketone, aldehyde) is not provided. ν(C=N): A peak at 3228 $cm^{-1}$ is attributed to the azomethine (C=N) functional group, indicating the presence of a nitrogen-carbon double bond in the compound. ν(N-O): A peak at 1617 $cm^{-1}$ corresponds to the nitro (N-O) group, suggesting stretching vibrations of nitrogen-oxygen bonds within the nitro group. ν(Ar): Peaks at 1561, 753, and 1456 $cm^{-1}$ suggest the presence of aromatic rings. These peaks are associated with stretching vibrations of the aromatic C-H bonds. ν($SO_4$): Peaks at 1148, 1052, 1030, 1132, and 670 $cm^{-1}$ suggest the presence of sulfate ($SO_4$) groups. These peaks are associated with specific stretching vibrations of these functional groups. υ(M-O): A peak at 611 $cm^{-1}$ indicates metal-oxygen stretching vibrations. This suggests the possible coordination of a metal ion with oxygen atoms in the compound. υ(M-N): A range from 566 to 528 $cm^{-1}$ corresponds to metal-nitrogen stretching vibrations. This implies the involvement of a metal-nitrogen coordination bond within the compound. In summary, the IR spectra data for Compound (4) indicates the presence of water, hydroxyl, carbonyl, azomethine, nitro, aromatic, sulfate, groups. Hydrogen bonding and metal coordination are suggested by specific peaks in the spectrum. The detailed information regarding various functional groups enhances the characterization of Compound (4), respectively, [17]. [Charts 5-9]. The provided IR spectra data corresponds to ligand $H_3L_2$, represents specific vibrational modes associated with various functional groups within the compound. Let's discuss the information provided: ν($H_2O$): No information is provided for the ν($H_2O$) peak. ν(OH): Peaks at 3436, 3355, and 1310 $cm^{-1}$ represent the hydroxyl (OH) group. The higher-frequency peaks indicate the stretching vibrations of free hydroxyl groups, while the lower-frequency peaks may indicate hydrogen-bonded hydroxyl groups. υ(H-bonding): Peaks at 3450, 3150, and 2721 $cm^{-1}$ suggest the involvement of

hydrogen bonding. These peaks are characteristic of compounds where hydrogen atoms are engaged in hydrogen bonding interactions. ν(C=O): A peak at 3170 $cm^{-1}$ indicates the presence of a carbonyl (C=O) group. The specific nature of the carbonyl functionality (e.g., ketone, aldehyde) is not provided. ν(C=N): A peak at 1661 $cm^{-1}$ is attributed to the azomethine (C=N) functional group, indicating the presence of a nitrogen-carbon double bond in the compound. ν(N-O): A peak at 1612 $cm^{-1}$ corresponds to the nitro (N-O) group, suggesting stretching vibrations of nitrogen-oxygen bonds within the nitro group. ν(Ar): Peaks at 1478, 750, and 1442 $cm^{-1}$ suggest the presence of aromatic rings. These peaks are associated with stretching vibrations of the aromatic C-H bonds. In summary, the IR spectra data for $H_3L_2$ indicates the presence of hydroxyl, carbonyl, azomethine, nitro, and aromatic groups. Hydrogen bonding and metal coordination information are not provided in this dataset. The presence of specific functional groups contributes to the characterization of $H_3L_2$. The provided IR spectra data corresponds to Compound (5), represents specific vibrational modes associated with various functional groups within the compound. Let's discuss the information provided: ν($H_2O$): Peaks at 3520, 3225, 3210, and 2840 $cm^{-1}$ indicate the presence of water. These peaks suggest stretching vibrations of water molecules within the compound. ν(OH): Peaks at 3414, 3266, and 1299, and 1249 $cm^{-1}$ represent the hydroxyl (OH) group. The higher-frequency peaks indicate the stretching vibrations of free hydroxyl groups, while the lower-frequency peaks may indicate hydrogen-bonded hydroxyl groups. υ(H-bonding): Peaks at 3720, 3310, 3165, and 2435 $cm^{-1}$ suggest the involvement of hydrogen bonding. These peaks are characteristic of compounds where hydrogen atoms are engaged in hydrogen bonding interactions. ν(C=O): A peak at 3270 $cm^{-1}$ indicates the presence of a carbonyl (C=O) group. The specific nature of the carbonyl functionality (e.g., ketone, aldehyde) is not provided. ν(C=N): The presence of an azomethine (C=N) group is suggested by a peak at 1631 $cm^{-1}$. ν(N-O): A peak at 1605 $cm^{-1}$ corresponds to the nitro (N-O) group, suggesting stretching vibrations of nitrogen-oxygen bonds within the nitro group. ν(Ar): Peaks at 1504, 755, and 1448 $cm^{-1}$ suggest the presence of aromatic rings. These peaks are associated with stretching vibrations of the aromatic C-H bonds. ν(OAc): Peaks at 1420 and 1333 $cm^{-1}$ suggest the presence of functional groups such as acetate (OAc). These peaks are associated with specific stretching vibrations of these functional groups. υ(M-O): A peak at 624 $cm^{-1}$ indicates metal-oxygen stretching vibrations. This suggests the possible coordination of a metal ion with oxygen atoms in the compound. υ(M-N): A peak at 530 $cm^{-1}$ corresponds to metal-nitrogen stretching vibrations. This implies the involvement of a metal-nitrogen coordination bond within the compound. In summary, the IR spectra data for Compound (5) indicates the presence of water, hydroxyl, carbonyl, azomethine, nitro, aromatic, acetate groups. Hydrogen bonding and metal coordination are suggested by specific peaks in the spectrum. The detailed information regarding various functional groups enhances the characterization of Compound (5). The provided IR spectra data corresponds to Compound (6), represents specific vibrational modes associated with various functional groups within the compound. Let's discuss the information provided: ν($H_2O$): Peaks at 3520, 3365, 3256, and 3125 $cm^{-1}$ indicate the presence of water. These peaks suggest stretching vibrations of water molecules within the compound. ν(OH): Peaks at 3490, 3339, and 1320, and 1296 $cm^{-1}$ represent the hydroxyl (OH) group. The higher-frequency peaks indicate the stretching vibrations of free hydroxyl groups, while the lower-frequency peaks may indicate hydrogen-bonded hydroxyl groups. υ(H-bonding): Peaks at 3710, 3105, 3785, and 2650 $cm^{-1}$ suggest the involvement of hydrogen bonding. These peaks are characteristic of compounds where hydrogen atoms are engaged in hydrogen bonding interactions. ν(C=O): A peak at 3221 $cm^{-1}$ indicates the presence of a carbonyl (C=O) group. The specific nature of the carbonyl functionality (e.g., ketone, aldehyde) is not provided. ν(C=N): The presence of an azomethine (C=N) group is suggested by a peak at 1660 $cm^{-1}$. ν(N-O): A peak at 1610 $cm^{-1}$ corresponds to the nitro (N-O) group, suggesting stretching vibrations of nitrogen-oxygen bonds within the nitro group. ν(Ar): Peaks at 1477, 759, and 1410 $cm^{-1}$ suggest the presence of aromatic rings. These peaks are associated with stretching vibrations of the aromatic C-H bonds. ν(Cl): A peak at 450 $cm^{-1}$ suggests the presence of functional groups such as chloride (Cl). This peak is associated with specific stretching vibrations of these functional groups. υ(M-O): A peak at 656 $cm^{-1}$ indicates metal-oxygen stretching vibrations. This suggests the possible coordination of a metal ion with oxygen atoms in the compound. υ(M-N): A peak at 530 $cm^{-1}$ corresponds to metal-nitrogen stretching vibrations. This implies the involvement of a metal-nitrogen coordination bond within the compound. In summary, the IR spectra data for Compound (6) indicates the presence of water, hydroxyl, carbonyl, azomethine, nitro, aromatic, chloride groups. Hydrogen bonding and metal coordination are suggested by specific peaks in the spectrum. The detailed information regarding various functional groups enhances the characterization of Compound (6). respectively [12]. [Charts 10-12**]**

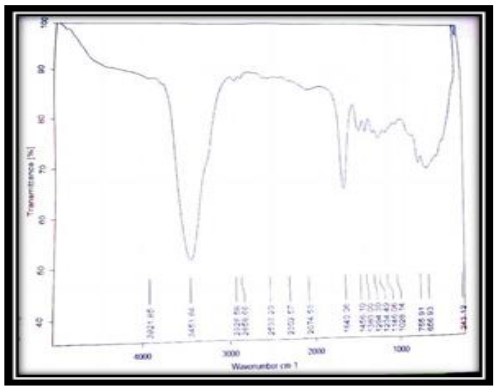


**Chart 5:** IR spectrum of ligand[$H_3L_1$]

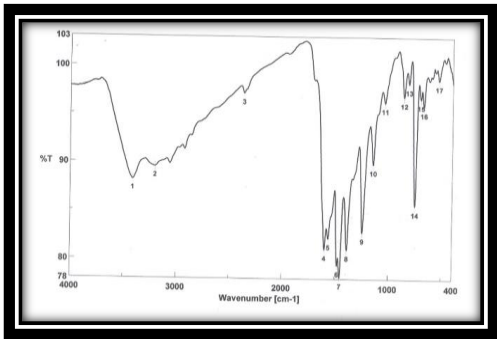


**Chart 6:** IR spectrum of Cu (II)complex (1)

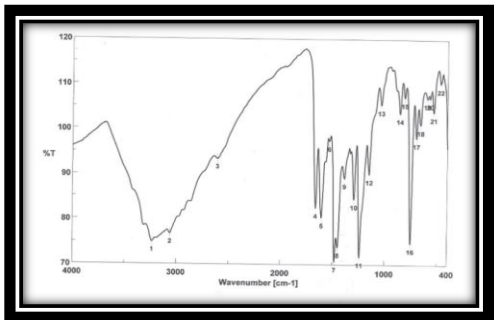


**Chart 7:** IR spectrum of Cu( II) complex (2)

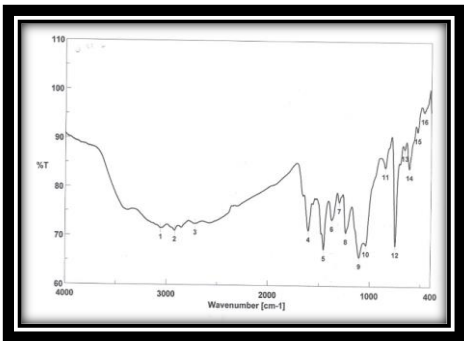


**Chart 8:** IR spectrum of Ag (I) complex (3)

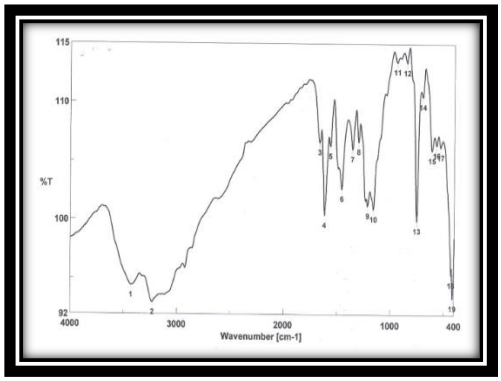


**Chart 9:** IR spectrum of Hg (II)complex (4)

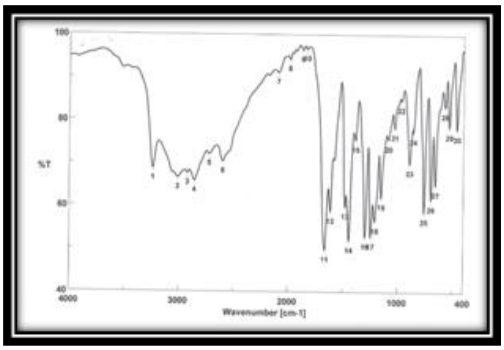


**Chart 10:** IR spectrum of ligand [$H_3L_2$]

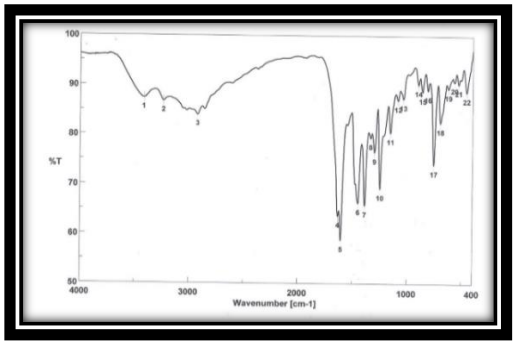


**Chart 11:** IR spectrum of Cu (II) complex (5)

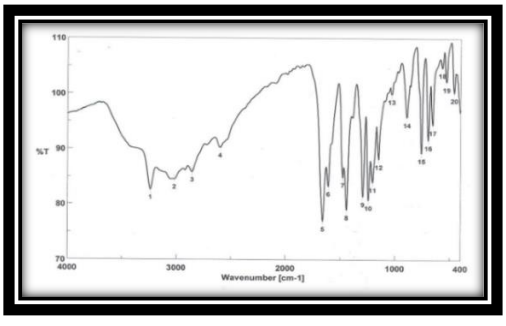


**Chart 12:** IR spectrum of Cu (II) complex (6)

**Table 4:** IR Frequencies of the Bands ($cm^{-1}$) of Ligands [$H_3L_1$], [$H_3L_2$] and their Metal Complexes

| No. | ν ($H_2O$) | ν(OH) | υ(H-bonding) | ν(C=O) | ν(C=N) | ν(N-O) | ν(Ar) | ν(OAc/$SO_4$/Cl/$NH_4$) | υ(M-O) | υ(M-N) |
|---|---|---|---|---|---|---|---|---|---|---|
| (1) | 3550,3250,3230 , 2940 | 3409,3389,1246 | 3615,3375,3270,2885 | 1650 | 3200 | 1609 | 1455,752,1470,700 | 1405,1365 | 672 | 531 |
| (2) | 3475,3310,3300 , 3090 | 3448,3395,1297,1243 | 3565,3240,3280,2710 | 1665 | 3234 | 1610 | 1535,752,1480,700 | 466 | 665 | 596 |
| (3) | 3585,3265,3220 , 2998 | 3410,3285,1300,1238 | 3615,3305, 3300,2465 | 1644 | 3258 | 1602 | 1498,750,1465,658 | 1105,1038,1050,690 | 613 | |
| (4) | 3550,3310,3300 ,3095 | 3427,3385,1355,1298 | 3610,3385,3370,2455 | 1661 | 3228 | 1617 | 1561,753,1456,696 | 1148,1052,1030,1132, 670 | 611 | 566-528 |
| (5) | 3520,3225,3210 , 2840 | 3414,3266,1299,1249 | 3720,3310,3165,2435 | 3270 | 1631 | 1605 | 1504,755,1448,732 | 1420,1333 | 624 | 530 |
| (6) | 3520,3365,3256 , 3125 | 3490,3339,1320,1296 | 3710,3105,3785,2650 | 3221 | 1660 | 1610 | 1477,759,1410,740 | 450 | 656 | 530 |

### 4.6. Electronic transition

The electronic absorption data of ligands and their complexes in dimethyl formamide (DMF), emphasizing changes in absorption bands and their implications on complex formation and coordination geometries. Here's a revised version: In Table 4, we present the electronic absorption data for both ligands and their complexes in dimethyl formamide (DMF). The initial absorption band is tentatively attributed to the $\pi \rightarrow \pi^*$ transition, which remains largely unchanged upon complexation. However, the subsequent band is associated with $n \rightarrow \pi^*$ and charge transfer transitions involving the azomethine and carbonyl groups [26]. Upon complex formation, these bands shift to lower energy levels, suggesting the involvement of these groups in coordination with the metal ions. The electronic spectra of copper(II) complexes (1) and (2) exhibit nearly identical features, with bands observed in the ranges of 288-287, 305-300, 449-429, 580-572, and 600-620 nm. While the first two bands are attributed to intraligand transitions, the others correspond to $2B_1g \rightarrow 2A_1g$ $\upsilon_1(dx^2\text{-}y^2 \rightarrow dz^2)$, $2B \rightarrow 2B_2g$ $\upsilon_2(dx^2\text{-}y^2 \rightarrow d_{xy})$, and $2B_1g \rightarrow 2Eg$ $\upsilon_3(dx^2\text{-}y^2 \rightarrow d_{xy}, d_{yz})$ transitions. These transitions suggest a tetragonally distorted octahedral geometry for the copper(II) ion, likely influenced by the Jahn-Teller effect on its $d^9$ electronic ground state [27, 28]. The magnetic moments for these copper(II) complexes at room temperature fall within the 1.69-1.74 range in Bohr magnetons (BM), supporting the notion of octahedral geometry [29]. Conversely, the absorption bands observed for Silver(I) complex (3) and Mercury(II) complex (4) (Table 5) are attributed to interligand transitions within the ligand, indicating diamagnetic properties [16]. For the second ligand, similar assignments hold true for the absorption bands, with shifts to lower energy levels upon complex formation indicating coordination with metal ions [30]. The electronic spectra of copper(II) complexes

(5) and (6) display bands within the ranges of 290-292, 306-305, 310-308, 360-365, 465-472, 560-570, and 615-610 nm. Again, these transitions suggest a tetragonally distorted octahedral geometry for the copper(II) ion, with magnetic moments falling within the 1.71-1.70 BM range at room temperature [29]. Additionally, electronic spectra for some metal complexes are depicted in charts [13-17] (Table 5).

**Table 5.** The electronic absorption spectral bands (nm) and magnetic moments (B.M.) for the ligands [$H_3L_1$], ($H_3L_2$) and their complexes

| No. | $\lambda_{max}$ (nm) | $\mu_{eff}$ in B.M. |
|---|---|---|
| ($H_3L_1$) | 290 nm (log ε =3.98), 310 nm ( log ε =4.25) | - |
| (1) | 288,305,449,580,600 | 1.70 |
| (2) | 287,300,429,572,620 | 1.71 |
| (3) | 289,305,322 | Diamag. |
| (4) | 289,305,325 | Diamag. |
| ($H_3L_2$) | 295,310,325 | - |
| (5) | 290,306,310,360,465,560,615 | 1.71 |
| (6) | 292,305,308,365,472,570,610 | 1.70 |

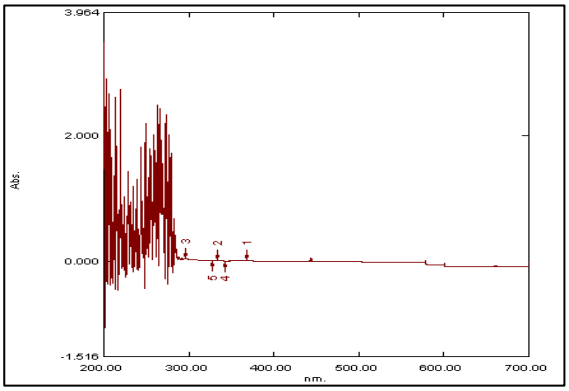


**Chart 13:** Electronic spectrum of Cu(II) complex (1)

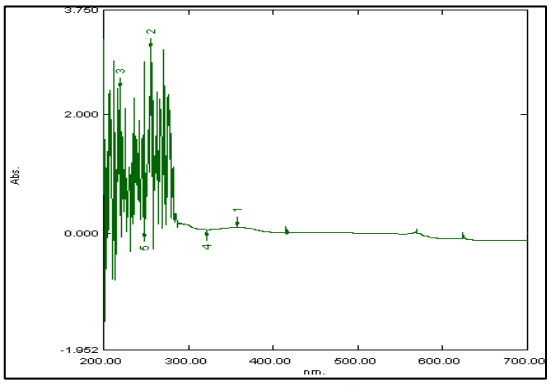


**Chart (14):** Electronic spectrum of Cu(II) complex (2)

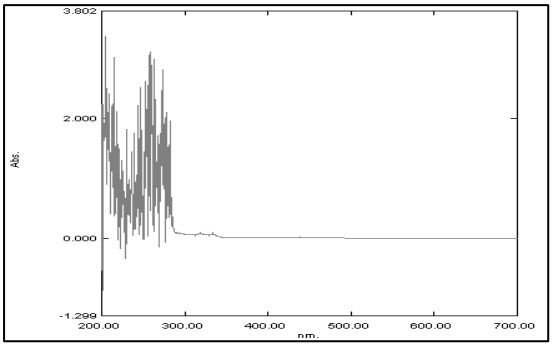


**Chart 15:** Electronic spectrum of Ag (I) complex (3)

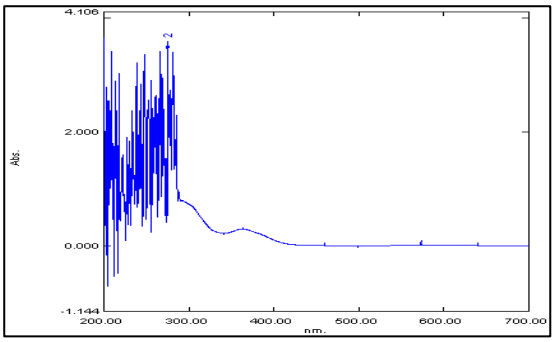


**Chart 16:** Electronic spectrum of Cu (II) complex (5)

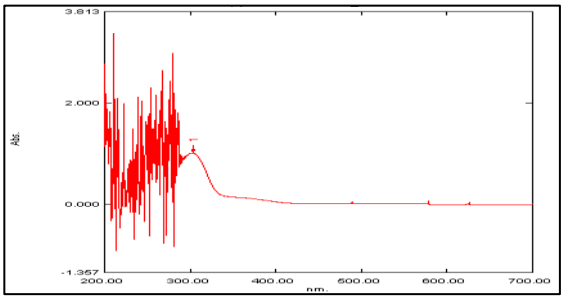


**Chart 17:** Electronic spectrum of Cu (II) complex (6)

### 4.7. Electron spin resonance (ESR)

To gain deeper insights into the stereochemistry and metal-ligand bonding nature, we conducted ESR spectra analysis on solid copper(II) complexes (1) and (2) (refer to Table 6). The spectra revealed anisotropic signals characterized by g values, with g‖ values of 2.15 and 2.11, and $g_\perp$ values of 2.05 and 2.02, respectively. These values are indicative of a $d^9$ configuration with an axial symmetry type of $d(x^2-y^2)$ ground state. Specifically, the g‖ and $g_\perp$ values being closer to 2.00, and $g_{\|} > g_\perp > g_e$ (2.0023), suggest a tetragonal distortion in the copper(II) complexes, corresponding to elongation along the four-fold symmetry z-axis [31, 32]. Moreover, the ratio of $g_{\|}/A_{\|}$ serves as a diagnostic tool for stereochemistry. Literature suggests this quotient as an empirical index of geometry, with reported ranges of 105-135 $cm^{-1}$ for square-planar complexes and 150-250 $cm^{-1}$ for tetrahedrally distorted complexes [33, 34]. The $g_{\|}/A_{\|}$ values for our chelates fall within the range (215-211), expected for tetragonally distorted octahedral copper(II) complexes [31, 35]. Additionally, the exchange coupling interaction between copper(II) ions is elucidated using the Hathaway expression: $G = (g_{\|} - 2) / (g_\perp - 2)$ [12, 33, 36, 37]. A G value greater than four implies negligible exchange interaction, while a value less than four indicates a considerable interaction in solid complexes. For copper(II) complex (1), the G value is 3.0 [Table 6], suggesting the presence of interaction between copper(II) ions. Conversely, for complex (2), its value is 5.5, indicating negligible exchange interactions between ions. Further insights come from Kivelson and Neiman's observation that in an ionic environment, $g_{\|}$ is typically 2.3 or larger, whereas in a covalent environment, $g_{\|}$ is less than 2.3. Given that the values of our complexes are less than 2.3, significant covalence in the metal-ligand bonding is implied [38, 39]. Calculations of the σ-parameter ($\alpha^2$) were derived from the following equations

$$\alpha^2 = (g_{\|} - 2.0023) + 3/7(g_\perp - 2.0023) - (P) + 0.04 \quad \ldots (1)$$

In the equations, P represents the free ion dipolar term, which is fixed at 0.036, while A‖ denotes the parallel coupling constant expressed in $cm^{-1}$. The $\alpha^2$ values for the copper complexes fall within the range of 0.49-0.44 [refer to Table 6]. These values point towards a notable presence of in-plane σ covalence [12, 40-42].

$$K_{||}^2 = (g_{||} - 2.0023)\Delta E_{xz} / 8\lambda_o \quad \ldots\ldots (2)$$

$$K_\perp^2 = (g_\perp - 2.0023)\Delta E_{xy} / 2\lambda_o \quad \ldots\ldots (3)$$

$$K^2 = (k_{||}^2 + 2k_\perp^2)/3 \quad \ldots\ldots (4)$$

In the equations, $\lambda_o$ represents the spin-orbit coupling of the free copper ion (-828 $cm^{-1}$), while $\Delta E_{xy}$ and $\Delta E_{xz}$ stand for the electronic transition energies of $2B_1 \rightarrow 2B_2$ and $2B_1 \rightarrow 2E$, respectively. To facilitate calculation, it was assumed that the peak maxima in the bands correspond to $\Delta E_{xy}$, and $\Delta E_{xz}$ can be inferred from the wavelengths of these bands. By utilizing the above relationships, we can compute the orbital reduction factors ($K_{//}$, $K_\perp$, and K), which serve as indicators of covalence. In an ionic environment, K equals 1, whereas in a covalent environment, K is less than 1; a lower K value suggests a higher degree of covalent character. The K values for the copper complexes are less than one, indicative of a considerable covalent bond character. The coefficients for plane and out-of-plane π-bonding ( and ) are contingent upon the values of $\Delta E_{xy}$ and $\Delta E_{xz}$ in the following equations:

$$\alpha^2\beta^2 = (g_\perp - 2.002)\Delta E_{xy} / 2\lambda_o \quad \ldots\ldots (5)$$

$$\alpha^2\beta_1^2 = (g_{||} - 2.002)\Delta E_{xz} / 8\lambda_o \quad \ldots\ldots (6)$$

The copper complexes exhibit values within the range of 0.79 to 0.68, indicating a moderate degree of covalent character in the in-plane π-bonding, while $\beta_2$ is 1.28 for complex (1) Chart (18), suggesting ionic character in the out-of-plane π-bonding. However, for complex (2) Chart (19), $\beta_2$ shows a value of 0.57, which is less than 0.83, indicating a covalent character. Turning to the second ligand, we conducted further analysis on the stereochemistry and metal-ligand bonding nature through ESR spectra of solid copper(II) complexes (5) Chart (20) and (6) (refer to Table 6). The spectra displayed anisotropic signals characterized by g values, with g‖ values of 2.21, 2.16, and g⊥ values of 2.06, 2.04, respectively. These values are characteristic of a species with a $d^9$ configuration and axial symmetry type of $d(x^2-y^2)$ ground state. The g‖ and $g_\perp$ values being closer to 2.00, and $g_{//} > g_\perp >$ ge (2.0023), suggest a tetragonal distortion in the copper(II) complexes, corresponding to elongation along the four-fold symmetry z-axis [45-50]. Furthermore, the $g_{//}/A_{//}$ ratio serves as a diagnostic tool for stereochemistry. It has been suggested that this quotient may be utilized as an empirical index of geometry, with reported ranges of 105-135 $cm^{-1}$ for square-planar complexes and 150-250 $cm^{-1}$ for tetrahedrally distorted chelates. The $g_{//}/A_{//}$ values for the complexes under consideration fall within the expected range for tetragonally distorted octahedral copper(II) complexes [43]. Additionally, the exchange coupling interaction between copper(II) ions can be elucidated using the Hathaway expression: $G = (g_{//} - 2) / (g_\perp - 2)$. A G value greater than four suggests negligible exchange interaction, while a value less than four indicates a considerable interaction in solid complexes. For copper(II) complex (5), the G value is 3.5 [Table 7], implying the presence of interaction between copper(II) ions. Conversely, for complex (6), its value is 4.0, indicating negligible exchange interactions between ions. Furthermore, Kivelson and Neiman noted that in an ionic environment, g‖ is typically 2.3 or larger, whereas in a covalent environment, g‖ is less than 2.3. Given that the values of our complexes are less than 2.3, significant covalence in the metal-ligand bonding is implied. The σ-parameter ($\alpha^2$) was calculated from the following equations

$$\alpha^2 = (g_{\|} - 2.0023) + 3/7(g_\perp - 2.0023) - (P) + 0.04 \quad \ldots\ldots (1)$$

In the equations, P represents the free ion dipolar term, fixed at 0.036, while $A_{//}$` denotes the parallel coupling constant expressed in $cm^{-1}$. The $\alpha^2$ values for the copper complexes fall within the range of 0.28 - 0.56 [refer to Table 6]. These values suggest the presence of a significant degree of in-plane σ covalence[39].

$$K_{||}^2 = (g_{||} - 2.0023)\Delta E_{xz} / 8\lambda_o$$
…… (2)

$$K_{\perp}^2 = (g_{\perp} - 2.0023)\Delta E_{xy} / 2\lambda_o$$
…… (3)

$$K^2 = (k_{||}^2 + 2k_{\perp}^2)/3$$
…… (4)

In the given context, $\lambda_o$ represents the spin-orbit coupling of the free copper ion (-828 $cm^{-1}$), while $\Delta E_{xy}$ and $\Delta E_{xz}$ denote the electronic transition energies of $2B_1 \rightarrow 2B_2$ and $2B_1 \rightarrow 2E$, respectively [41]. For calculation purposes, it was assumed that the peak maxima in the band correspond to $\Delta E_{xy}$, and $\Delta E_{xz}$ can be inferred from the wavelength of these bands. Utilizing the above relationships, we can calculate the orbital reduction factors ($K_{//}$, $K_{\perp}$, and K), which serve as indicators of covalence [44]. In an ionic environment, K equals 1, whereas in a covalent environment, K is less than 1; a lower K value indicates a greater covalent character. The values of K for the copper complexes are less than one, suggesting a considerable covalent bond character. The coefficients for plane and out-of-plane π-bonding (and) depend on the values of $\Delta E_{xy}$ and $\Delta E_{xz}$ in the following equations:

$$\alpha^2\beta^2 = (g_{\perp} - 2.002)\Delta E_{xy} / 2\lambda_o$$
…… (5)

$$\alpha^2\beta_1^2 = (g_{||} - 2.002)\Delta E_{xz} / 8\lambda_o$$
…… (6)

The copper complexes exhibited values within the range of 1.0 to 0.86, indicating a moderate degree of covalent character in the in-plane π-bonding. Meanwhile, $\beta_2$ values ranged from 1.34 to 0.98, suggesting ionic character in the out-of-plane π-bonding.

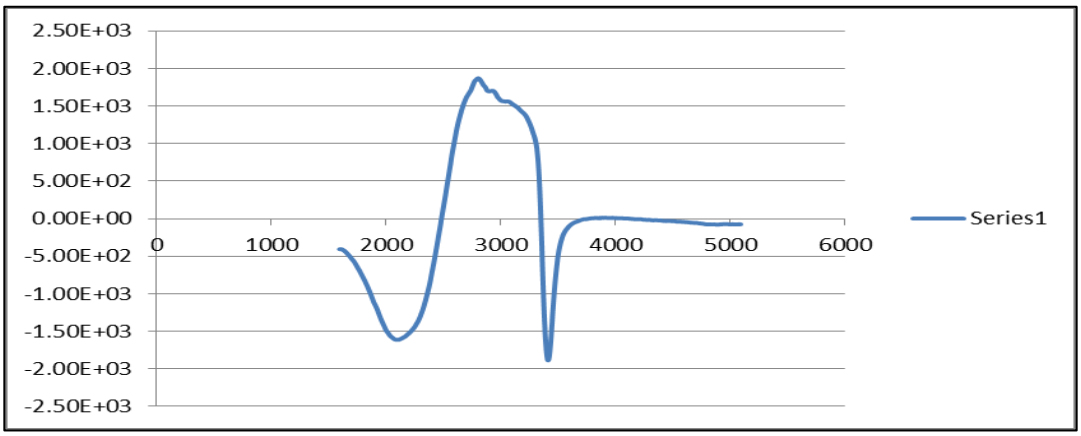


**Chart 18:** ESR spectrum of Cu (II) complex (1)

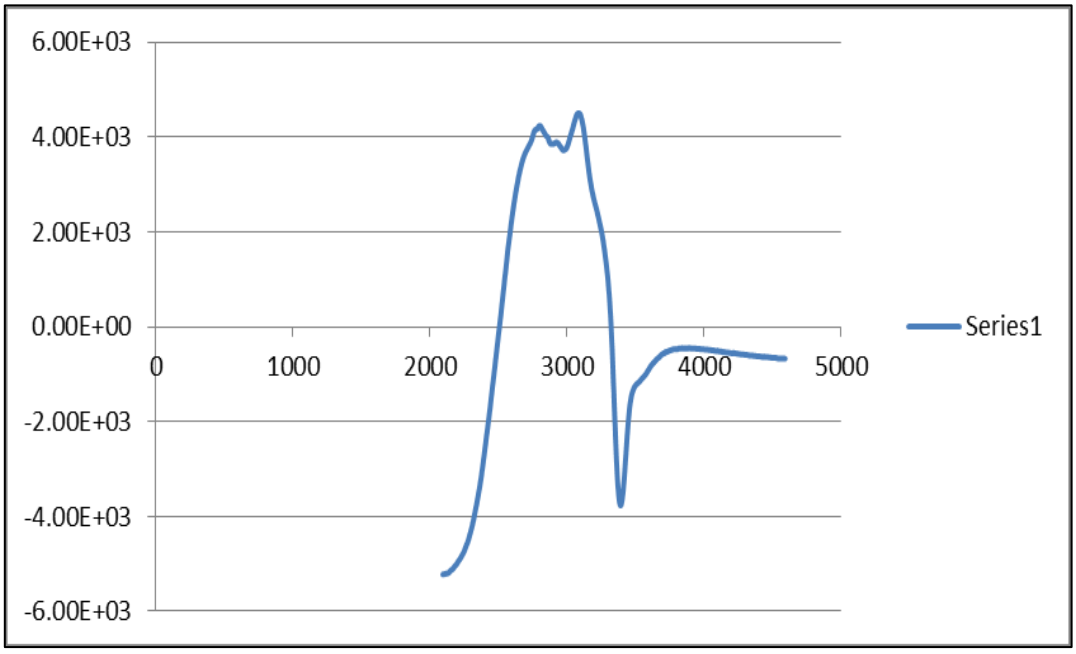


**Chart 19:** ESR spectrum of **Cu** (II) complex (2)

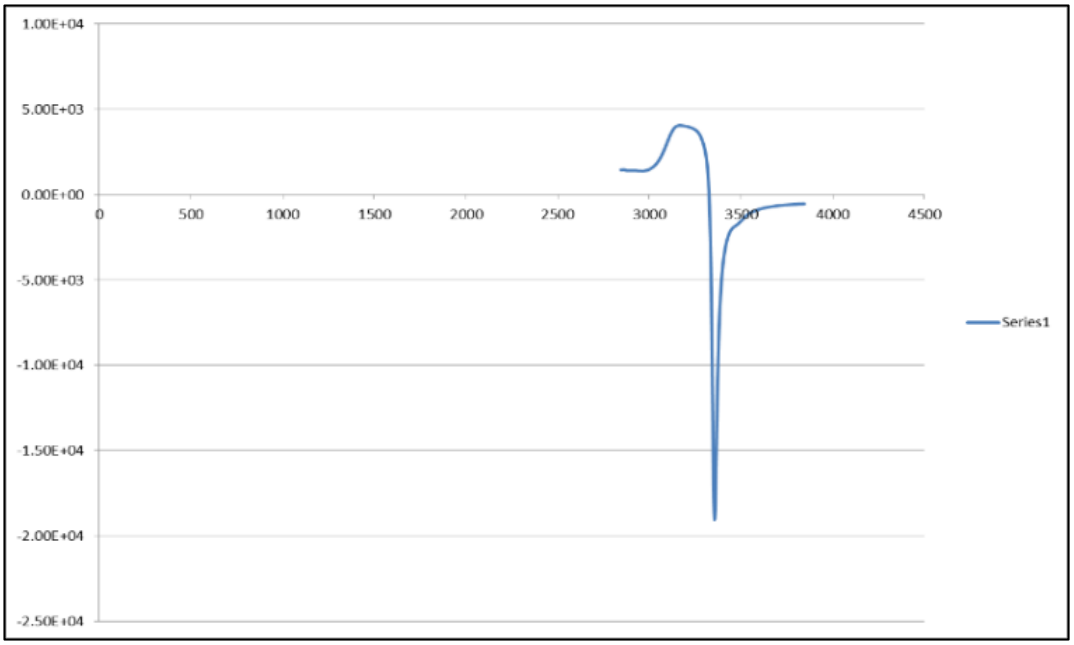


**Chart 20:** ESR spectrum of Cu (II) complex (5)

**Table 6.** ESR data for the metal (II) complexes of ligand [$H_3L_1$] and ligand [$H_3L_2$].

| No. | $g_{\parallel}$ | $g_{\perp}$ | gisoa | $A_{\parallel}$ (G) | $A_{\perp}$ (G) | Aisob (G) | G c | $\Delta E_{xy}$ | $\Delta E_{xz}$ | $K_{\perp}^2$ | $K_{\parallel}^2$ | K | $K^2$ | $g_{\parallel}/A_{\parallel}$ | $\alpha^2$ | $ß_2$ | $ß_1^2$ | -2 ß | ad2 (%) |
|---|---|---|---|---|---|---|---|---|---|---|---|---|---|---|---|---|---|---|---|
| (1) | 2.15 | 2.05 | 2.08 | 95 | 5 | 35 | 3.0 | 17699 | 21978 | 0.63 | 0.39 | 0.74 | 0.55 | 215 | 0.49 | 1.28 | 0.79 | 175.7 | 74.74 |
| (2) | 2.11 | 2.02 | 2.05 | 105 | 10 | 41.7 | 5.5 | 18248 | 22988 | 0.25 | 0.3 | 0.51 | 0.27 | 211 | 0.44 | 0.57 | 0.68 | 183.4 | 78.03 |
| (5) | 2.21 | 2.06 | 2.11 | 100 | 10 | 40 | 3.5 | 17857 | 21505 | 0.75 | 0.56 | 0.82 | 0.68 | 221 | 0.56 | 1.34 | 1.0 | 222.2 | 94.5 |
| (6) | 2.16 | 2.04 | 2.08 | 120 | 7.5 | 45 | 4.0 | 17857 | 21505 | 0.49 | 0.43 | 0.69 | 0.47 | 216 | 0.28 | 0.98 | 0.86 | 226.03 | 96.2 |

a) giso = $(2g_{\perp} + g_{\parallel})/3$, b) Aiso = $(2A_{\perp} + A_{\parallel})/3$, c) G= $(g_{\parallel} - 2)/ (g_{\perp} - 2)$

### 4.8. Thermal analyses

The thermal data of the chelates are given in [Table 7]. Such data corroborate the stoichiometric formula, number of water molecules, and end products. TG-DTA curves of complexes (3) and (6), were introduced as representative examples. The thermo gram of Complex (3) [$H_3L_1Ag_2(SO_4)$] exhibited multiple decomposition steps, the first step involving breaking of H-bonding accompanied with endothermic peak at 48 $^oC$. In the second step, by 14.7 % (Calcd 14.9 %) weight loss accompanied by an endothermic peak at 280 $^oC$ was assigned to loss of one sulfate group ($SO_4$). The endothermic peak observed at 330 $^oC$ refers to the melting point of the complex. The final step observed as exothermic peaks at 385-470-670 $^0C$ ranges with 42.5 % weight loss (Calcd 42.1 %), refers to complete oxidative decomposition of the chelate which ended up with the formation of $Ag_2O$. Complex (6) [$H_3L_2$ $CuCl_2$].3 $H_2O$ exhibited multiple decomposition steps, the first step involving breaking of H-bondings accompanied with endothermic peak at 49 $^oC$. In the second step, three molecules of hydrated water were lost endothermically with a peak at 80 $^oC$ accompanied by 11.51 % (Calcd 11.46 %) weight loss. 16.92 % (Calcd 16.78 %) weight loss accompanied by an endothermic peak observed at 148 $^oC$ was assigned to loss of 2 chloride atoms respectively ( 2 Cl) atoms. The endothermic peak observed at 320 $^oC$ refers to the melting point of the chelate. The final step observed a exothermic peaks at 290-410-540 $^oC$ ranges with 22.84 % weight loss (Calcd 22.76 %), refers to complete oxidative decomposition of the complex which ended up with the formation of CuO .

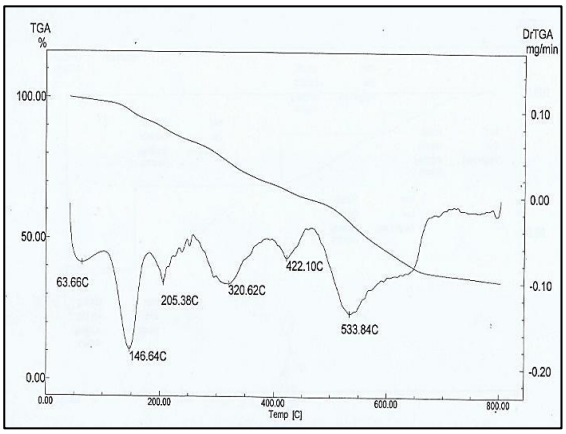


**Chart 21:** Thermogram of Ag (II) complex (3)

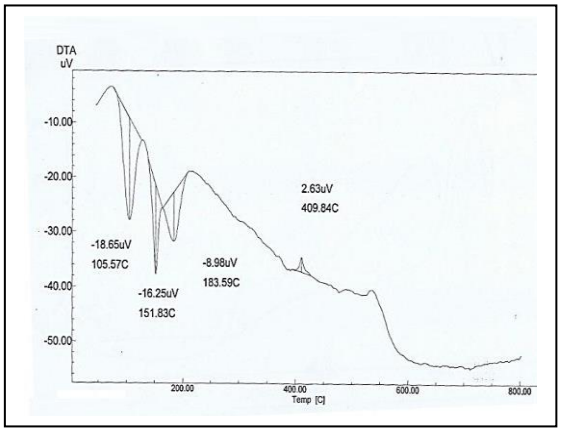


**Chart 22:** Thermogram of Cu (II) complex (6)

**Table 7:** Thermal analyses for metal (II) complexes of ligands(1),(2)

| Compound No. Molecular formula | Temp. ($^oC$) | DTA (peak) | | TGA (Wt. Loss %) | | Assignments |
|---|---|---|---|---|---|---|
| | | Endo | Exo | Calc. | Found | |
| L1. $AgSO_4$ Complex (3) | 48 | Endo | - | | | Broken of H-bonding |
| | 280 | Endo | - | 14.9 | 14.7 | Loss of ($SO_4$) group |
| | 330 | Endo | - | | | Melting point |
| | 385-470-670 | - | Exo | 42.1 | 42.5 | Decomposition process with the formation of $Ag_2O$ |
| | | | | | | |
| L2. $CuCl_2$ Complex (6) | 49 | Endo | - | | | Broken of H-bonding |
| | 80 | Endo | - | 11.46 | 11.51 | Loss of 3($H_2O$) hydrated water molecules |
| | 148 | Endo | - | 16.78 | 16.92 | Loss of2 (Cl)Atoms respectively |
| | 320 | - | Exo | | | Melting point |
| | 290-410-540 | - | Exo | 22.76 | 22.84 | Decomposition process with the formation of CuO |
| | 49 | Endo | - | | | Broken of H-bonding |

### 4.9. Transmission electron microscopy

Transmission Electron Microscopy (TEM) emerges as a powerful tool in the intricate domain of nanoscale material analysis. Its significance lies in its unmatched ability to provide detailed insights into the structure, morphology [45], and composition of specimens with exceptional resolution. This technique plays a crucial role in uncovering the mysteries of the minuscule world of materials. At the core of TEM's importance are its high-resolution imaging capabilities, which surpass those of traditional microscopes [42, 46]. Operating at scales beyond the capabilities of conventional microscopy, TEM delves into atomic and molecular landscapes, offering visualizations of structures at sub-nanometer precision [27, 47]. This remarkable resolution enables the exploration of fine details, presenting a visual narrative that reveals the atomic arrangements within a material [48]. TEM is indispensable in studying internal material structures, providing access to the exploration of crystalline configurations, defects, and grain boundaries. Its analytical prowess extends to fields such as nanotechnology, materials science, and medicine, where TEM serves as a vital tool for nanoparticle characterization. Through the combination of TEM with energy-dispersive X-ray spectroscopy (EDS), a comprehensive understanding of diverse specimens is achieved, elucidating biological intricacies and unveiling chemical compositions. In essence, TEM transcends conventional microscopy; it serves as a transformative force in scientific inquiry and technological advancement, driving progress across disciplines and revealing the unseen complexities of materials at the nanoscale [49]. The average diameter of particles in the tested complex was determined to be 29.02±5.02 nm. TEM samples for the colloidal suspension of the complexes in distilled water were meticulously prepared by depositing colloids onto carbon-coated TEM grids, allowing the liquid carrier to evaporate, and subsequently assaying them using a JEOL 1230 transmission electron microscope (120 kV) following the methodology outlined [50]. The results exhibited varying values for the tested complexes, with the Ag(I) complex (3) displaying the smallest size at 14.08 nm, followed by the Cu(II) complex (2) at 15.22 nm, the Cu(II) complex (6) at 19.22 nm, as illustrated in Figures (1-3). The complex particles were observed to be in the nano size range, within diameters ranging from 1 to 100 nm. Such nanoscale dimensions confer new or enhanced size-dependent properties compared to larger particles of the same material [49]. This offers several advantages, including increased bioavailability, dose proportionality, decreased toxicity, smaller dosage forms (e.g., smaller tablets), and stable dosage forms for drugs that are either unstable or have unacceptably low bioavailability in non-nano particulate forms. Furthermore, the increased surface area of the active agent results in faster dissolution in aqueous environments such as the human body, translating to greater bioavailability, smaller drug doses, reduced toxicity, and minimized fed/fasted variability [12, 38, 43, 51]

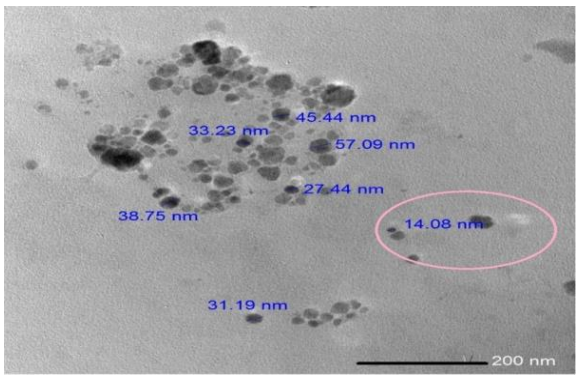


**Figure 1:** TEM images for Ag(I) complex (3) nanoparticles

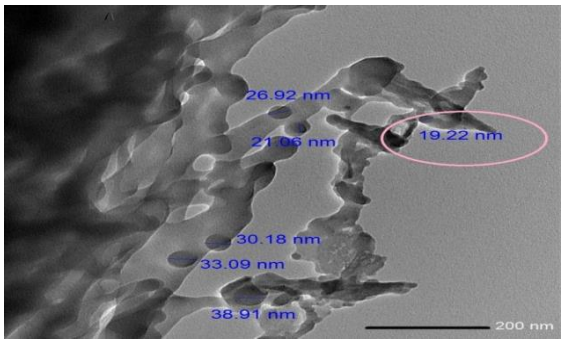


**Figure 2:** TEM images for Cu(II) complex (2) nanoparticles

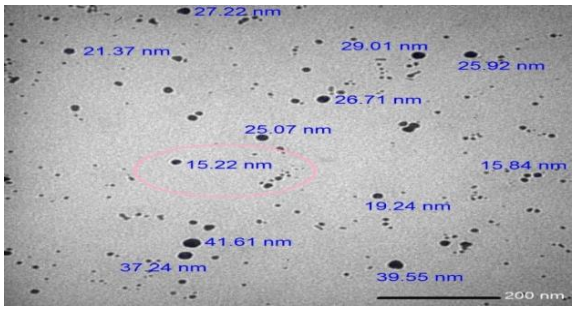


**Figure 3:** TEM images for Cu(II) complex(6) nanoparticles

### 4.10. The molecular formula

The results of elemental analyses, IR, $^{1}$H-NMR ,mass spectra, electronic absorption spectra, magnetic measurements as well as the electron spin resonance and the thermal analyses makes it possible to suggest the molecular formula for the studied complexes (Figure 4-11) [50, 52].

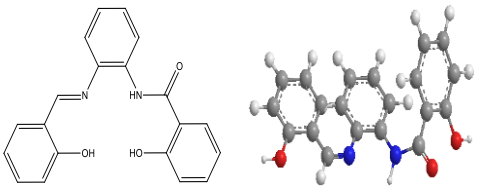

Figure (4): Ligand (1) [$H_3L_1$]

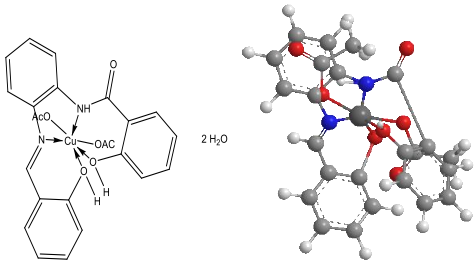

Figure (5): Complex(1)

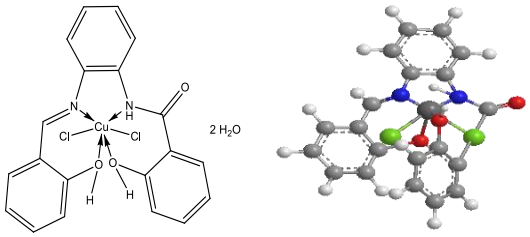

Figure (6): Complex (2)

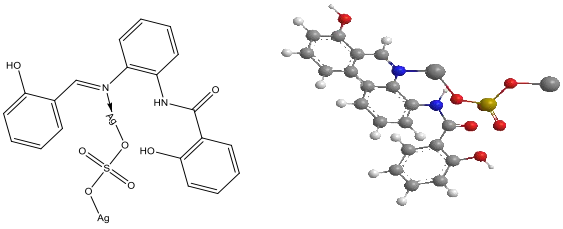

Figure (7): Complex (3)

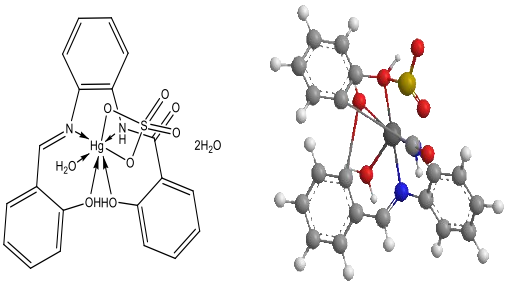

Figure (8): Complex (4)

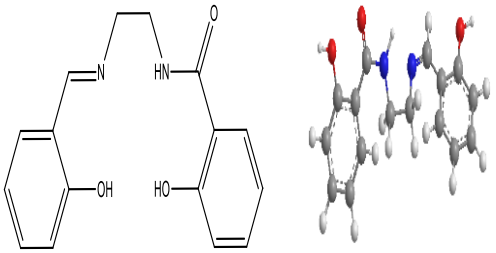

Figure (9): Ligand (2) [$H_3L_2$]

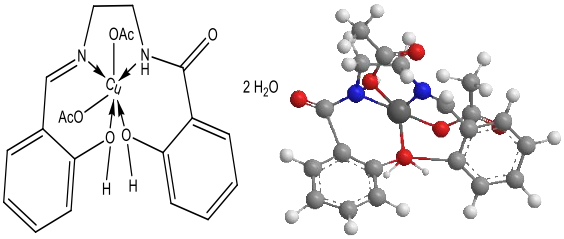

Figure (10): Complex (5)

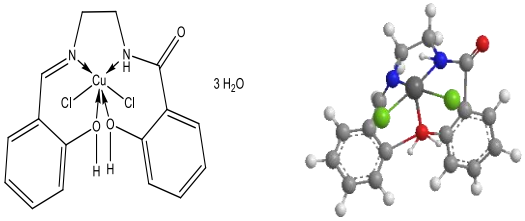

Figure (11): Complex (6)

**4.11. Biological activities**

This study focuses on the synthesis and antibacterial evaluation of the Schiff bases of amides-transition metal complexes with the aim of developing novel therapeutic agents. The study explores the design, synthesis, characterization, and antibacterial properties of these complexes, shedding light on their potential as effective antibacterial agents. The transition metal complexes were synthesized using various ligands and characterized using spectroscopic and analytical techniques [49].The increasing prevalence of antibiotic-resistant bacteria poses a significant threat to public health, emphasizing the urgent need for the development of alternative antibacterial agents [53]. Transition metal complexes have emerged as promising candidates due to their unique electronic and structural properties. This research aims to contribute to the field by synthesizing and evaluating the antibacterial activity of novel transition metal complexes.The transition metal complexes were synthesized through the reaction of selected metal ions with carefully chosen ligands. The ligands were designed to impart specific properties to the resulting complexes, such as potential target specificity. The synthesized complexes were characterized using various spectroscopic and analytical techniques, including UV-Vis spectroscopy, infrared spectroscopy, and elemental analysis [3, 5, 12, 54, 55]. In vitro biological screening tests of the ligand $H_3L_1$ and metal complexes and its metal complexes (1),(2),(3) and (4) in addition to the amid ligand $H_3L_2$ and its metal complexes (5) and (6) carried out as antibacterial and antifungal activity and presented in figure (12). The antimicrobial activity of tested compounds was determined using agar well diffusion method. All the compounds were tested in vitro for their antibacterial activity against Staphylococcus aureus and Streptococcus mutans (Gram positive bacteria), Escherichia coli, Pseudomonas aeruginosa and Klebsiella pneumonia (Gram negative bacteria) using nutrient agar medium. The antifungal activity of the tested compounds was tested against Candida albicans and Asperagillus niger using Sabouraud dextrose agar medium. Ampicillin and Gentamicin were used as standard drugs for Gram positive and Gram negative bacteria, respectively. Nystatin was used as a standard drug for fungi strains. DMSO was used as solvent (negative) control [8, 12, 38, 43, 51] . The compounds were tested at a concentration of 15 mg/ml against both bacterial and fungal strains(53). of ligand $H_3L_1$ and complexes Cu(II)(1), Cu(II)(2), Ag(I)(3) and Hg(II)(4) in addition to the of ligand $H_3L_2$ and complexes of Cu(II) (5), and Cu(II) (6) show antibacterial activity against Streptococcs mutans, Staphyliccus aureus, Klebsiella pneumonia and Escherichia coli [4]. The results showed that, the order of cytotoxic effect against Gram positive and Gram negative strains for Streptococcs mutans is: Standard drug>(4)>(3)>( $H_3L_1$)> (6)> (5)>(2)> (1)> ($H_3L_2$), for Staphyliccus aureus is : (4) >(3) >( $H_3L_1$) >(2) >Standard drug > (1) > (6) > ($H_3L_2$) > (5), for Klebsiella pneumonia is: Standard drug > (4) > (3) > ($H_3L_1$) > (2)> (6) > (1) > ($H_3L_2$) , also for Escherichia coli is: Standard drug > ($H_3L_1$) > (4) > (3) > (6) > (5) > (1) > ($H_3L_2$) . Hg(II) (4), Ag(I) (3), Cu(II)(1), Cu(II) (5), Cu(II) (6) and (Cu(II)(2), complexes showed wide range of bactericide activity against the gram positive and gram negative bacteria. The complexes were also subjected to antifungal activity against Candida albicans [49]. The investigation shows that, the order of cytotoxic effect against Candida albicans is : ($H_3L_1$) > (4) > (3) > Standard drug > ($H_3L_2$) > (6) > (5) >[ (2) and (1) are NA], Analysis of growth pattern of Candida albicans in presence of complexes reveals that, the complexes have potential the growth of fungus tested. Further, $H_3L_1$, Hg(II)(4), Ag(I)(3) complexes respectively are more active against Candida albicans. Also $H_3L_2$, Cu(II) (6), Cu(II) (5), complexes are moderately activity, and Cu (II) (2) and Cu(II)(1) complexes are inactive against Candida albicans. The zone of inhibition was measured with respect to control and results are presented in Table (8) and (Figure 12).

**Table (8):** mean inhibition zone of the standard drug, $H_3L_1$, $H_3L_2$ and their metal complexes against Escherichia coli (ATCC:10536), Klebsiella pneumonia (ATCC:10031), Staphylococcus aureus (ATCC:13565) and Streptococcus mutans (ATCC:25175)

| | Microorganism / complex | Gram negative bacteria | | Gram positive bacteria | | Fungi |
|---|---|---|---|---|---|---|
| | | Escherichia coli (ATCC:10536) | Klebsiella pneumonia (ATCC:10031) | Staphylococcus aureus (ATCC:13565) | Streptococcus mutans (ATCC:25175) | Candida albicans (ATCC:10231) |
| | Standard antibiotic | Gentamicin | Gentamicin | Ampicillin | Ampicillin | Nystatin |
| | | 27±0.5 | 25±0.5 | 20±0.1 | 30±0.5 | 21±0.5 |
| $L_1$ | $H_3L_1 = C_{20}H_{16}N_2O_3$ | 21.7±0.6 | 20.7±0.6 | 21.7±0.6 | 21.3±0.6 | 25.3±0.6 |
| **1** | $[H_3L_1.Cu(OAc)_2].2H_2O$ | 11.7±0.6 | 11.7±0.6 | 19.7±0.6 | 10.7±0.6 | NA |
| **2** | $[H_3L_1CuCl_2].2\ H_2O$ | NA | 13.7±0.6 | 20.7±0.6 | 12.3±0.6 | NA |
| **3** | $[H_3L_1Ag_2(SO_4)]$ | 17.7±0.6 | 21.7±0.6 | 23.7±0.6 | 22.3±0.6 | 21.7±0.6 |
| **4** | $[H_3L_1Hg(SO_4)(H_2O)].2\ H_2O$ | 20.7±0.6 | 24.7±0.6 | 28.7±0.6 | 25.7±0.6 | 23.3±0.6 |
| $L_2$ | $H3L2 = C_{16}H_{16}N_2O_3$ | 10.7±0.6 | 9.7±0.6 | 11.3±0.6 | 9.7±0.6 | 12.7±0.6 |
| **5** | $[H3L2\ Cu(OAc)_2].2H_2O$ | 13.7±0.6 | 9.7±0.6 | 10.3±0.6 | 13.3±0.6 | 10.3±0.6 |
| **6** | $[H3L2\ CuCl_2].3\ H_2O$ | 14.7±0.6 | 13.3±0.6 | 13.7±0.6 | 13.7±0.6 | 10.7±0.6 |

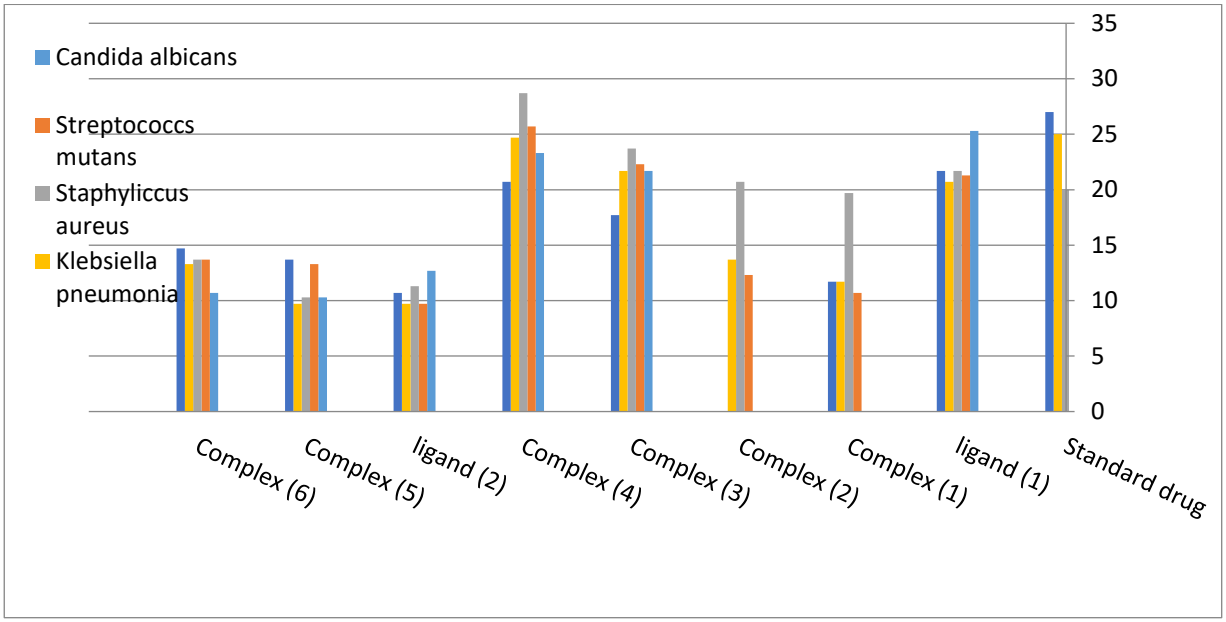


**Figure (12):** Mean inhibition zone of the standard drug, $H_3L_1$,$H_3L_2$ and their metal complexes against Escherichia coli (ATCC:10536), Klebsiella pneumonia (ATCC:10031), Staphylococcus aureus (ATCC:13565) and Streptococcus mutans (ATCC:25175)

## 5. Conclusions

The study delineates the cytotoxic effects of various complexes against both Gram-positive and Gram-negative bacterial strains, as well as Candida albicans. Notably, Hg(II), Ag(I), and Cu(II) complexes exhibited broad-spectrum bactericidal activity, while also demonstrating significant antifungal activity. The observed differences in activity, particularly against Candida albicans, were attributed to the nano volume of the complexes, with the aromatic $H_3L_1$ displaying higher potency compared to the aliphatic $H_3L_2$. These findings highlight the potential of nano-sized complexes as effective antimicrobial agents, underscoring their importance in therapeutic development against a range of microbial infections.

## 6. Conflicts of interest

"There are no conflicts to declare".

## 7. References


1. El Tabl, A., et al., Nano-organometallic complexes as therapeutic platforms against breast cancer cell lines;(in vitro study). 2021. 64(3): p. 1627-1637.
2. El-Tabl, A. S., Abd-El Wahed, M. M., Sayed Ahmed, R. A., Alhalib, A. A. A., &Ashour, A. M. (2022). Physico-chemical Characterization and Estimation of Antimicrobial Activity of Modified Aspirin in the form of Nano-organometallic Compounds. Chemical Science International Journal, 31(3), 11-37.
3. El-Tabl, A., et al., Potential Drugs Containing Amines As Representative Example Of Pharmaceutical And Biologically Active Compounds Section A-Research paper Potential Drugs Containing Amines As Representative Example Of Pharmaceutical And Biologically Active Compounds. 2023. 12: p. 3495-3531.
4. Nano-Organometallic Compounds as Prospective Metal BasedAnti-Lung Cancer Drugs: Biochemical and Molecular Docking Studies,El-Tabl, A. S., Kolkaila, S. A., Abdullah, S. M., & Ashour, A. M. (2023). TWIST, 18(4), 141-150
5. El-Tabl, A., et al., Novel Metal Complexes of Bioactive Amide Ligands as New Potential Antibreast Cancer Agents. 2023. 18: p. 151-169.
6. Artacho, J., et al., Twisted Amide Analogues of Tröger's Base. Chemistry – A European Journal, 2012. 18(4): p. 1038-1042.
7. Avaji, P.G., S.A. Patil, and P.S.J.T.M.C. Badami, Synthesis, spectral, thermal, solid-state DC electrical conductivity and biological studies of Co (II) complexes with Schiff bases derived from 3-substituted-4-amino-5-hydrazino-1, 2, 4-triazole and substituted salicylaldehydes. 2008. 33: p. 275-283.
8. Jayaprakash, R., et al., Antioxidant activity of ethanolic extract of Tinospora cordifolia on N-nitrosodiethylamine (diethylnitrosamine) induced liver cancer in male Wister albino rats. 2015. 7(Suppl 1): p. S40.
9. Bashore, C.G., et al., Twisted Amide Reduction under Wolff−Kishner Conditions: Synthesis of a Benzo-1-Aza-Adamantane Derivative. Journal of the American Chemical Society, 2003. 125(11): p. 3268-3272.
10. Bosch, F. and L.J.P. Rosich, The contributions of Paul Ehrlich to pharmacology: a tribute on the occasion of the centenary of his Nobel Prize. 2008. 82(3): p. 171-179.
11. The Cytotoxicity of Some Biologically Active Nano Compounds against Colon Cancer: Advanced Biochemical Analyses ,El-Tabl, A. S., Dawood , A. A. E. R. ., Kolkaila , S. ., Mohamed , E. H., & Ashour, A. (2023).. TWIST, 18(4), 360-371.
12. Abbasi, S.Y., et al. Effect of Carica papaya leaf juice on blood cell count of busulfan-induced chronic bone marrow aplasia in mice. in Proceedings. 2021.
13. Akhila, J.S., D. Shyamjith, and M.J.C.s. Alwar, Acute toxicity studies and determination of median lethal dose. 2007: p. 917-920.
14. Arnau, J., et al., Current strategies for the use of affinity tags and tag removal for the purification of recombinant proteins. 2006. 48(1): p. 1-13.
15. Bao, G., S. Mitragotri, and S.J.A.r.o.b.e. Tong, Multifunctional nanoparticles for drug delivery and molecular imaging. 2013. 15: p. 253-282.
16. Beilner, D., et al., Lysine-specific histone demethylase 1A (LSD1) in cervical cancer. 2020. 146: p. 2843-2850.
17. Bhat, M.A., et al., Carvone Schiff base of isoniazid as a novel antitumor agent: nanoemulsion development and pharmacokinetic evaluation. 2015. 203: p. 111-119.
18. Clayden, J., Book Review: The Amide Linkage Structural Significance in Chemistry, Biochemistry, and Materials Science. Edited by Arthur Greenberg, Curt M. Breneman and Joel F. Liebman. Angewandte Chemie-international Edition - ANGEW CHEM INT ED, 2003. 42: p. 1788-1789.
19. Correia, I., et al., Hydroxyquinoline derived vanadium(IV and V) and copper(II) complexes as potential anti-tuberculosis and anti-tumor agents. Journal of Inorganic Biochemistry, 2014. 141: p. 83-93.
20. El-Tabl, A.S., et al., Synthesis, spectroscopic characterization and biological activity of the metal complexes of the Schiff base derived from phenylaminoacetohydrazide and dibenzoylmethane. 2008. 71(1): p. 90-99.
21. Elsadek, B., et al., The antitumor activity of a lactosaminated albumin conjugate of doxorubicin in a chemically induced hepatocellular carcinoma rat model compared to sorafenib. 2017. 49(2): p. 213-222.
22. El-Tabl, A.S., et al., Synthesis, Spectroscopic Investigation and Biological Activity of Metal (ll) Complexes with N2O4 Ligands. 2009. 2009(9): p. 582-587.
23. El-Tabl, A.S.J.T.M.C., Synthesis and physico-chemical studies on cobalt (II), nickel (II) and copper (II) complexes of benzidine diacetyloxime. 2002. 27(2): p. 166-170.
24. Current Advances in Biological Activities of New Metal Complexes Bearing Aromatic

Hydroxy Schiff-base Ligand,Faheem, S. M. ., El-Tabl, A. S. ., Abd-El Wahed, M. M. ., Kaid, M., & Younes, S. M,TWIST Journal, 19(1), 36-57 (2024).

25. Pattabiraman, V.R. and J.W. Bode, Rethinking amide bond synthesis. (1476-4687 (Electronic)).
26. Kemnitz, C.R. and M.J.J.J.o.t.A.C.S. Loewen, "Amide resonance" correlates with a breadth of C− N rotation barriers. 2007. 129(9): p. 2521-2528.
27. Serag, H.M., M.M. El Komy, and H.S.J.T.E.J.o.H.M. Ahmed, Assessment the Role of Bisphenol A on Chemotherapeutic Efficacy of Cisplatin against Hepatocellular Carcinoma in Male Rats. 2019. 74(2): p. 352-363.
28. Shi, S., G. Meng, and M. Szostak, Synthesis of Biaryls through Nickel-Catalyzed Suzuki–Miyaura Coupling of Amides by Carbon–Nitrogen Bond Cleavage. Angewandte Chemie International Edition, 2016. 55(24): p. 6959-6963.
29. Brown, D.G. and J. Boström, Analysis of Past and Present Synthetic Methodologies on Medicinal Chemistry: Where Have All the New Reactions Gone? (1520-4804 (Electronic)).
30. G Novel Metal Complexes of Bioactive Amide Ligands as New Potential Antibreast Cancer Agents, El-Tabl, Abdou ,El-Wahed, Moshira,Kadi, Noha,Kolkaila, Sherif,Daba, Mohamed,twist Journal,vol.18,issue4,151-169,(2024)
31. Novel nano-metal complexes of modified aspirin as future antimicrobial agent, Abdou El Tabl, AbdEl-Hamid Ismail, Moshira Abd-El Wahed and Ahmed M.Ashour,International Journal of pharmatheutical Research ,Vol.14,Issue1,85-110 (2022).
32. Huang, Z., et al., The role of long noncoding RNAs in hepatocellular carcinoma. 2020. 19: p. 1-18.
33. Kosinska, A.D., et al., Synergy of therapeutic heterologous prime-boost hepatitis B vaccination with CpG-application to improve immune control of persistent HBV infection. 2019. 9(1): p. 10808.
34. Shi, S. and M. Szostak, Efficient Synthesis of Diaryl Ketones by Nickel-Catalyzed Negishi Cross-Coupling of Amides by Carbon–Nitrogen Bond Cleavage at Room Temperature Accelerated by a Solvent Effect. Chemistry – A European Journal, 2016. 22(30): p. 10420-10424.
35. Modulation of cancer therapy using nano-organometallic compounds: preparation, spectroscopic characterization and cytotoxic evaluation, Abdou El Tabl, Moshira Abd-El Wahed, Eman Mohamed, Mohammed Abu-Setta, Egyptian Journal of Chemistry, Vol.64, No.7, , PP 3873-3887(2021) .
36. Khaled, S., et al., Synthesis, characterization, and photophysical studies of some novel ruthenium (II) polypyridine complexes derived from benzothiazolyl hydrazones. 2013.
37. Ali, S. G., El Tabl, A. S., Shabana, A. A., Abd-El Wahed, M. M., Ashour, A. M.,Abu-Setta, M. H.H. &Elzaref A. S. (2023). Recent advances in metal complexes of new multifunctional ether ligand as potential anti-breast cancer agents. European Chemical Bulletin, 12 (5), 1464-1514
38. Jarenmark, M., et al., Unsymmetrical dizinc complexes as models for the active sites of phosphohydrolases. 2010. 39(35): p. 8183-8194.
39. Love, J., et al., JASP: Graphical statistical software for common statistical designs. 2019. 88: p. 1-17.
40. El Tabl, A. S., Abd-El Wahed, M. M., Ashour, A. M., Aly, A. A., Abu-Setta, M. H.H. (2023). Recent advances in metal complexes of new multifunctional ether ligand as potential anti-breast cancer agents. European Chemical Bulletin,12 (5), 1436-1463
41. Wang, B. and Z.J.C.A.E.J. Cao, Acid-Catalyzed Reactions of Twisted Amides in Water Solution: Competition between Hydration and Hydrolysis. 2011. 17(42): p. 11919-11929.
42. Whitehead Jr, R.D., et al., Methods and analyzers for hemoglobin measurement in clinical laboratories and field settings. 2019. 1450(1): p. 147-171.
43. Kaspar, A.A. and J.M. Reichert, Future directions for peptide therapeutics development. Drug Discov Today, 2013. 18(17-18): p. 807-17.
44. Hie, L., et al., Conversion of amides to esters by the nickel-catalysed activation of amide C–N bonds. Nature, 2015. 524(7563): p. 79-83.
45. Zoubi, W.A., F. Kandil, and M.J.O.C.C.R. Chebani, Synthesis of macrocyclic schiff bases based on pyridine-2, 6-dicarbohydrazide and their use in metal cations extraction. 2012. 1(104): p. 2161-0401.1000104.
46. El Tabl, A. S., Abu-Setta, M. H.H., Ashour, A. M., El-Afify, N. F., &Batakoushy, H. A. (2023). Organometallic ester compounds as a promising source of new antimicrobial drugs. Egyptian Journal of Chemistry
47. Meng, G. and M. Szostak, General Olefin Synthesis by the Palladium-Catalyzed Heck

Reaction of Amides: Sterically Controlled Chemoselective N□C Activation. Angewandte Chemie International Edition, 2015. 54(48): p. 14518-14522.
48. Brunton, L.L., B.A. Chabner, and B.C. Knollmann, in Goodman & Gilman's: The Pharmacological Basis of Therapeutics, 12e. 2015, McGraw-Hill Education: New York, NY.
49. Feng, G., et al., A highly reactive mononuclear Zn (II) complex for phosphodiester cleavage. 2005. 127(39): p. 13470-13471.
50. Kirby, A.J., I.V. Komarov, and N. Feeder, Synthesis, structure and reactions of the most twisted amide. Journal of the Chemical Society, Perkin Transactions 2, 2001(4): p. 522-529.
51. El-Tabl, A.S., Abd-El Wahed, M. M., Abu-Setta, M.H.H., El-Mahsarawy, A.I., &Ashour, A.M (2022). Cytotoxicity and antitumor activity of organometallic copper (II) Nano particles in a chemically induced hepatocellular carcinoma rat model.International Journal of Pharmaceutical Sciences and Research, Vol.14 (3): 1000-11
52. Meng, G. and M. Szostak, Palladium-catalyzed Suzuki–Miyaura coupling of amides by carbon–nitrogen cleavage: general strategy for amide N–C bond activation. Organic & Biomolecular Chemistry, 2016. 14(24): p. 5690-5707.
53. Li, X. and G. Zou, Acylative Suzuki coupling of amides: acyl-nitrogen activation via synergy of independently modifiable activating groups. Chemical Communications, 2015. 51(24): p. 5089-5092.
54. Meng, G. and M. Szostak, Rhodium-Catalyzed C–H Bond Functionalization with Amides by Double C–H/C–N Bond Activation. Organic Letters, 2016. 18(4): p. 796-799.
55. El-Tabl, A.S., et al., Synthesis of novel metal complexes with isonicotinoyl hydrazide and their antibacterial activity. 2010. 34(2): p. 88-91.